International Journal for Numerical Methods in Engineering

WILEY

RESEARCH ARTICLE OPEN ACCESS

Two New Calibration Techniques of Lumped-Parameter Mathematical Models for the Cardiovascular System

Andrea Tonini[1] | Francesco Regazzoni[1] | Matteo Salvador[2] | Luca Dede'[1] | Roberto Scrofani[3] | Laura Fusini[4] | Chiara Cogliati[5,6] | Gianluca Pontone[4] | Christian Vergara[7] | Alfio Quarteroni[1,8]

[1]MOX, Dipartimento di Matematica, Politecnico di Milano, Milan, Italy | [2]Institute for Computational and Mathematical Engineering, Stanford University, Palo Alto, California, USA | [3]UOC Cardiochirurgia Fondazione IRCCS Ca' Granda, Ospedale Maggiore Policlinico di Milano, Milan, Italy | [4]Centro Cardiologico Monzino IRCCS, Milan, Italy | [5]Internal Medicine, Luigi Sacco Hospital, Milan, Italy | [6]Department of Biomedical and Clinical Sciences, Università di Milano, Milan, Italy | [7]LABS, Dipartimento di Chimica, Materiali e Ingegneria Chimica, Politecnico di Milano, Milan, Italy | [8](Professor Emeritus) Institute of Mathematics, Ecole Polytechnique Fédérale de Lausanne, Lausanne, Switzerland

Correspondence: Andrea Tonini (andrea.tonini@polimi.it)

Received: 17 May 2024 | **Revised:** 10 October 2024 | **Accepted:** 2 December 2024

Funding: This work has been funded by the Italian research project FISR (Fondo Integrativo Speciale per la Ricerca) 2020 "Mathematical modeling of Covid-19 effects on the cardiac function, Mathematical modeling and analysis of clinical data related to the Covid-19 pandemic in Italy, 2021_ASSEGNI_DMAT_10". Funding agency: MIUR (Italian Ministry of Education, Universities and Research).

Keywords: cardiocirculatory models | global sensitivity analysis | optimization | parameter estimation

ABSTRACT

Cardiocirculatory mathematical models are valuable tools for investigating both physiological and pathological conditions of the circulatory system. To assess an individual's clinical condition, these models must be tailored through parameter calibration. This study introduces a novel calibration method for a lumped-parameter cardiocirculatory model, by leveraging on the correlation matrix between model parameters and outputs to adjust the latter based on observed data. We evaluate the performance of our method, both independently and in combination with the L-BFGS-B optimization algorithm (Limited memory Broyden–Fletcher–Goldfarb–Shanno with Bound constraints), and we compare our results with those of L-BFGS-B alone. Using synthetic data, we show that both the correlation matrix calibration method and the combined one reduce the loss function of the optimization problem more effectively than L-BFGS-B. Moreover, the correlation matrix calibration method exhibits greater robustness to the initial parameter guess than both the combined method and L-BFGS-B. When applied to noisy data, all three calibration methods achieve comparable results. Although the correlation matrix calibration method yields less accurate parameter estimates than L-BFGS-B, in a real-world clinical case, the two new calibration methods provide clinical insights comparable to L-BFGS-B. Notably, the correlation matrix calibration method is three times faster than the other two calibration methods. These findings highlight the effectiveness of our new calibration method for clinical applications.

Abbreviations: BSA, body surface area; **CI**, cardiac index; **CMC**, correlation matrix calibration method; **CMC-L-BFGS-B**, hybrid calibration method between the correlation matrix calibration method and L-BFGS-B; **CO**, cardiac output; **HR**, heart rate; $\mathbf{LA}_{\mathrm{Pmax}}$, maximal left atrial pressure; $\mathbf{LA}_{\mathrm{Pmean}}$, mean left atrial pressure; $\mathbf{LA}_{\mathrm{Pmin}}$, minimal left atrial pressure; $\mathbf{LA}_{\mathrm{Vmax}}$, maximal left atrial volume; **L-BFGS-B**, Limited memory Broyden–Fletcher–Goldfarb–Shanno with Bound constraints; $\mathbf{LV}_{\mathrm{EDV}}$, left ventricular end diastolic volume; $\mathbf{LV}_{\mathrm{EF}}$, left ventricular ejection fraction; $\mathbf{LV}_{\mathrm{ESV}}$, left ventricular end systolic volume; $\mathbf{LV}_{\mathrm{Pmax}}$, maximal left ventricular pressure; $\mathbf{LV}_{\mathrm{Pmin}}$, minimal left ventricular pressure; $\mathbf{LV}_{\mathrm{SV}}$, left ventricular stroke volume; $\mathbf{max}\,\nabla\,\mathbf{P}_{\mathrm{rAV}}$, maximal right atrioventricular pressure gradient; **ODE**, ordinary differential equations; $\mathbf{PAP}_{\mathrm{max}}$, systolic pulmonary arterial pressure; $\mathbf{PAP}_{\mathrm{mean}}$, mean pulmonary arterial pressure; $\mathbf{PAP}_{\mathrm{min}}$, diastolic pulmonary arterial pressure; **PVR**, pulmonary vascular resistance; $\mathbf{PWP}_{mean}$, mean pulmonary wedge pressure; $\mathbf{PWP}_{min}$, minimal pulmonary wedge pressure; $\mathbf{RA}_{\mathrm{Pmean}}$, mean right atrial pressure; $\mathbf{RA}_{\mathrm{Pmax}}$, maximal right atrial pressure; $\mathbf{RA}_{\mathrm{Pmin}}$, minimal right atrial pressure; $\mathbf{RA}_{\mathrm{Vmax}}$, maximal right atrial volume; $\mathbf{RV}_{\mathrm{EDV}}$, right ventricular end diastolic volume; $\mathbf{RV}_{\mathrm{EF}}$, right ventricular ejection fraction; $\mathbf{RV}_{\mathrm{ESV}}$, right ventricular end systolic volume; $\mathbf{RV}_{\mathrm{Pmax}}$, maximal right ventricular pressure; $\mathbf{RV}_{\mathrm{Pmin}}$, minimal right ventricular pressure; $\mathbf{SAP}_{\mathrm{max}}$, systolic systemic arterial pressure; $\mathbf{SAP}_{\mathrm{min}}$, diastolic systemic arterial pressure; **SVR**, systemic vascular resistance.

1 | Introduction

Cardiocirculatory mathematical models have been developed to simulate both physiological and pathological conditions within the human body [1–8]. *Lumped-parameter* or 0D models partition the cardiovascular system into reduced compartments (e.g., systemic arteries or left atrium), where only average flow rates and pressures are computed over time. Each compartment is characterized by a set of parameters (e.g., resistances of the vessels or elastances of the cardiac chambers) that typically represent average, physiological conditions. Lumped-parameter models are also referred to as 0D because they do not depend on spatial variables.

Calibration methods adjust the parameters of lumped-parameter cardiocirculatory models to minimize the distance between model outputs and either in silico or clinical data, making the models patient-specific [3, 9]. Previous studies have shown the advantages of deterministic calibration methods for these models using synthetic data. For example, Laubscher et al. [10] employed a combination of the Adam optimizer and L-BFGS-B [11, 12] (Limited memory Broyden–Fletcher–Goldfarb–Shanno with Bound constraints) to estimate parameters influencing the left ventricular pressure-volume loop, while Bjørdalsbakke et al. [13–15] utilized a trust region reflective algorithm following sensitivity analysis for different estimation scenarios. These studies relied on gradient-based calibration methods. Nguyen and Bui–Thanh [16], in a pioneering work, theoretically analyzed variational autoencoders for parameter estimation. Within the Bayesian framework, Saxton et al. [17] used an Unscented Kalman filter to estimate parameters of a cardiocirculatory model that accounts for the left ventricle and for systemic circulation with a time-varying heartbeat period. Markov Chain Monte Carlo (MCMC) methods have shown potential in determining the posterior distribution of parameters, despite suffering from the curse of dimensionality [18]. Advances in MCMC, including adaptive MCMC, improved efficiency [19]. Argus et al. [20] combined sensitivity analysis and parallel MCMC for cardiocirculatory parameter estimation. Moreover, variational [21] and amortized [22] inference techniques are viable approaches to estimate the posterior distribution of parameters. Goh et al. [22] theoretically analyzed the convergence properties of the latent states of a specific variational autoencoder to the statistics of the posterior distribution.

In this study, we focus on the deterministic framework and propose a novel gradient-free calibration method for lumped-parameter cardiocirculatory models. This method leverages on the correlation matrix between model parameters and outputs to surrogate the gradient of the loss function. We refer to this method as *Correlation Matrix Calibration* method (CMC). We identify parameters significantly affecting a set of model outputs, corresponding to available data (such as the maximal left atrial volume or the systemic systolic arterial pressure), through global sensitivity analysis [23, 24] (GSA). These identified parameters are then calibrated.

We compare the proposed CMC to the L-BFGS-B [11, 12] optimization algorithm using a dataset of in silico-generated data. Additionally, we introduce a hybrid calibration method (CMC-L-BFGS-B) to achieve enhanced accuracy. This hybrid approach applies CMC for global calibration, followed by L-BFGS-B for local refinement. Although we limit our analysis to cardiocirculatory lumped-parameter models, our approach is general and can be applied to other problems as well.

To further validate CMC and CMC-L-BFGS-B, we apply them to patient-specific data related to COVID-19 pneumonia provided by Centro Cardiologico Monzino and L. Sacco Hospital in Milan, Italy. In severe COVID-19 pneumonia, right ventricular dysfunction, characterized by dilation, reduced function, and elevated pulmonary arterial pressure, is strongly associated with mortality, while left ventricular involvement is less common [25–27]. Additionally, endothelial damage with diffuse micro-thrombosis, leading to increased pulmonary resistance and reduced compliance, has been documented in histological studies [28, 29]. We define parameter ranges for the calibration procedure based on these observations.

The outline of this paper is as follows: Section 2 describes the lumped-parameter cardiocirculatory model, its parameters and model outputs; Section 3 presents the GSA and the considered calibration methods; Section 4 tests the robustness of the calibration methods on both in silico-generated and patient-specific data; Section 5 draws the conclusions of this work.

2 | Lumped-Parameter Cardiocirculatory Model

This section introduces the lumped-parameter cardiocirculatory model, detailing its parameters and outputs.

A lumped-parameter cardiocirculatory model represents the human cardiovascular system as an electrical circuit: blood flow through vessels and valves is analogous to electrical current, blood pressure to electric potential, resistance to blood flow corresponds to electrical resistance, vessel compliance is modeled as electrical capacitance and blood inertia is represented by inductance.

The model partitions the cardiovascular system into distinct compartments (e.g., right atrium, systemic arteries/veins). Each compartment is described by a system of ordinary differential equations (ODE) [1–3] that capture the time evolution of model variables, like pressures, flow rates, and cardiac volumes.

Our proposed lumped-parameter model builds upon the work of Regazzoni et al. [30], incorporating additional compartments to represent the systemic and pulmonary microvasculature (Figure 1).

The model includes the four cardiac chambers and divides the systemic and pulmonary circulations into arterial, capillary, and venous compartments. Specifically, we model the pulmonary microcirculation using two compartments for oxygenated and non-oxygenated capillaries because some pulmonary capillaries do not oxygenate due to hypoxic vasoconstriction in alveoli with low oxygen concentration, even if lung perfusion is normal. The fraction of blood that does not oxygenate is called the pulmonary shunt. In healthy individuals, the pulmonary shunt is typically below 5% [31], but it can increases up to 60% in conditions such as

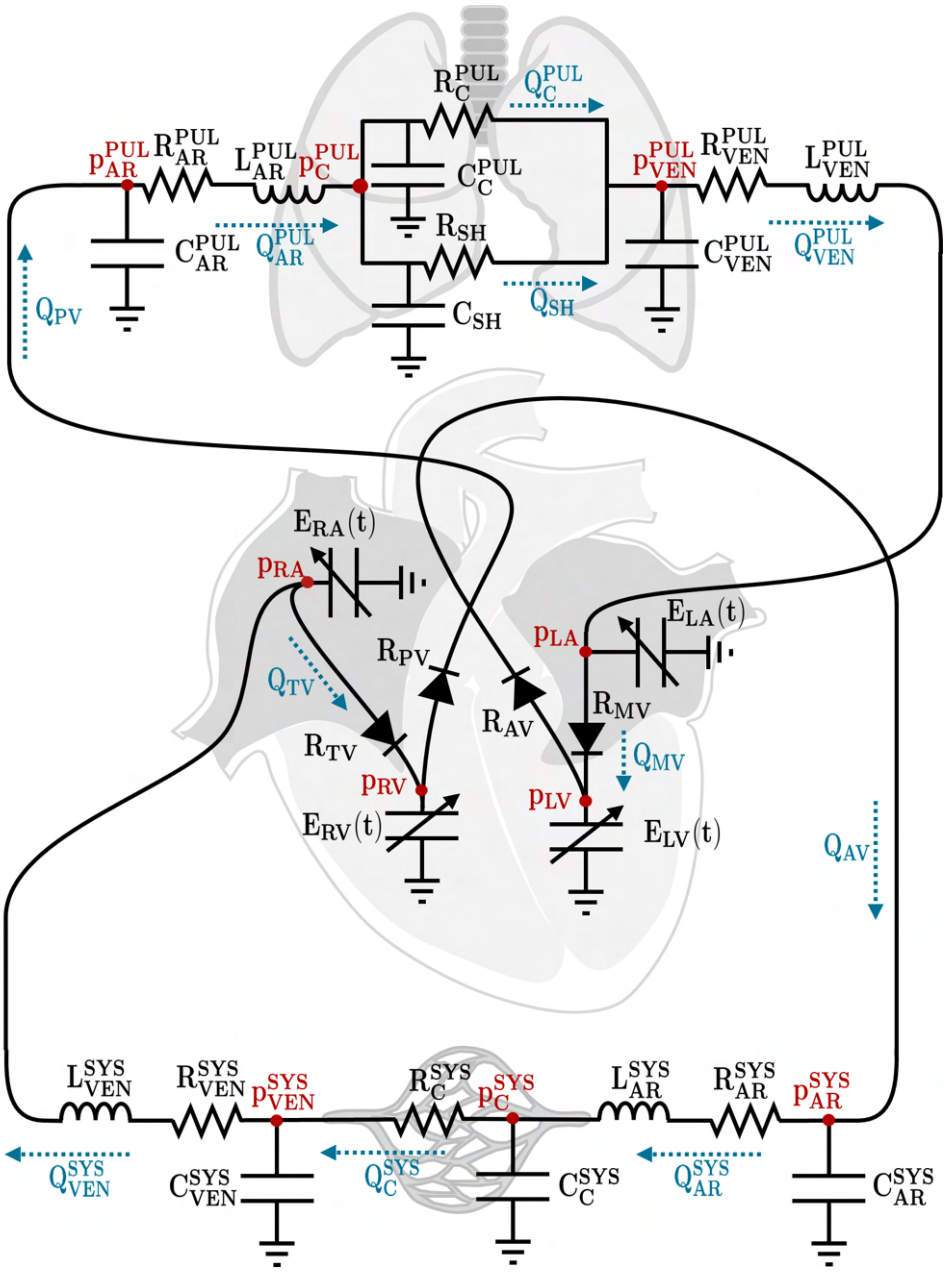

FIGURE 1 | Lumped-parameter model. We depict pressures and flow rates in red and blue, respectively, and parameters in black.

acute respiratory distress sindromes, as COVID-19 [32, 33]. The hemodynamic of the cardiovascular system is described by the following dynamical system:

$$\begin{cases} \dot{\mathbf{x}}(t;\mathbf{x}_0,\mathbf{p}) = \mathbf{f}(t,\mathbf{x}(t;\mathbf{x}_0,\mathbf{p});\mathbf{p}) & t \in (0,T] \\ \mathbf{x}(0;\mathbf{x}_0,\mathbf{p}) = \mathbf{x}_0 \end{cases} \tag{1}$$

where $\mathbf{x}$, $\mathbf{x}_0$, $\mathbf{p}$, $\mathbf{f}$, and T represent the state variables, initial conditions, model parameters, the system right-hand side (rhs) and the final time, respectively. Moreover, we calculate additional quantities $\mathbf{y}$, referred to as model outputs, which are functions (e.g., the maximum or the mean) of the state variables $\mathbf{x}$ and parameters $\mathbf{p}$:

$$\mathbf{y} = \mathbf{g}(\mathbf{x}(t;\mathbf{x}_0,\mathbf{p});\mathbf{p})$$

The state variables $\mathbf{x}$ of our model include:

- The volumes of the left atrium (V_{LA}) and ventricle (V_{LV}) and of the right atrium (V_{RA}) and ventricle (V_{RV}).
- The circulatory pressures of the systemic arteries (p_{AR}^{SYS}), capillaries (p_C^{SYS}) and veins (p_{VEN}^{SYS}) and of the pulmonary arteries (p_{AR}^{PUL}), capillaries (p_C^{PUL}) and veins (p_{VEN}^{PUL}).
- The circulatory fluxes of the systemic arteries (Q_{AR}^{SYS}) and veins (Q_{VEN}^{SYS}) and of the pulmonary arteries (Q_{AR}^{PUL}) and veins (Q_{VEN}^{PUL}).

The model depends on the heart rate (HR), which determines the heartbeat period $T_{HB} = 60/HR$, and on the parameters $\mathbf{p}$ reported in Table 1. We set the final time $T = 25T_{HB}$ to reach the limit cycle of the dynamical system.

TABLE 1 | List of parameters and their reference values for an ideal healthy individual. The reference values of the parameters, excluding HR [34], are adapted from literature values [3, 35], to ensure that the model outputs $\mathbf{y}$ fall within echocardiographic ranges related to a healthy individual (Table 2).

	Parameter	Unit	Reference value	Description
Parameters used in the global sensitivity analysis	EA_{LA}	mmHg/mL	0.38	Left atrial active elastance
	EB_{LA}	mmHg/mL	0.27	Left atrial passive elastance
	$V_{U,\mathrm{LA}}$	mL	2.31	Left atrial unloaded volume
	EA_{LV}	mmHg/mL	2.7	Left ventricular active elastance
	EB_{LV}	mmHg/mL	0.069	Left ventricular passive elastance
	$V_{U,\mathrm{LV}}$	mL	3.54	Left ventricular unloaded volume
	EA_{RA}	mmHg/mL	0.13	Right atrial active elastance
	EB_{RA}	mmHg/mL	0.20	Right atrial passive elastance
	$V_{U,\mathrm{RA}}$	mL	3.54	Right atrial unloaded volume
	EA_{RV}	mmHg/mL	0.43	Right ventricular active elastance
	EB_{RV}	mmHg/mL	0.041	Right ventricular passive elastance
	$V_{U,\mathrm{RV}}$	mL	8.41	Right ventricular unloaded volume
	R_{min}	mmHg· s/mL	0.0063	Minimal valve resistance
	R_{max}	mmHg· s/mL	94168	Maximal valve resistance
	$R_{\mathrm{AR}}^{\mathrm{SYS}}$	mmHg· s/mL	0.59	Systemic arterial resistance
	$C_{\mathrm{AR}}^{\mathrm{SYS}}$	mL/mmHg	1.33	Systemic arterial compliance
	$L_{\mathrm{AR}}^{\mathrm{SYS}}$	mmHg · s^2/mL	0.00021	Systemic arterial inertia
	$R_{\mathrm{C}}^{\mathrm{SYS}}$	mmHg· s/mL	0.022	Systemic capillary resistance
	$C_{\mathrm{C}}^{\mathrm{SYS}}$	mL/mmHg	0.28	Systemic capillary compliance
	$R_{\mathrm{VEN}}^{\mathrm{SYS}}$	mmHg· s/mL	0.36	Systemic venous resistance
	$C_{\mathrm{VEN}}^{\mathrm{SYS}}$	mL/mmHg	75	Systemic venous compliance
	$L_{\mathrm{VEN}}^{\mathrm{SYS}}$	mmHg · s^2/mL	0.000021	Systemic venous inertia
	$R_{\mathrm{AR}}^{\mathrm{PUL}}$	mmHg· s/mL	0.071	Pulmonary arterial resistance
	$C_{\mathrm{AR}}^{\mathrm{PUL}}$	mL/mmHg	6.0	Pulmonary arterial compliance
	$L_{\mathrm{AR}}^{\mathrm{PUL}}$	mmHg · s^2/mL	0.000021	Pulmonary arterial inertia
	$R_{\mathrm{C}}^{\mathrm{PUL}}$	mmHg· s/mL	0.018	Oxygenated pulmonary capillary resistance
	$C_{\mathrm{C}}^{\mathrm{PUL}}$	mL/mmHg	5.78	Oxygenated pulmonary capillary compliance
	R_{SH}	mmHg· s/mL	0.35	Non-oxygenated pulmonary capillary resistance
	C_{SH}	mL/mmHg	0.049	Non-oxygenated pulmonary capillary compliance
	$R_{\mathrm{VEN}}^{\mathrm{PUL}}$	mmHg· s/mL	0.038	Pulmonary venous resistance
	$C_{\mathrm{VEN}}^{\mathrm{PUL}}$	mL/mmHg	13.18	Pulmonary venous compliance
	$L_{\mathrm{VEN}}^{\mathrm{PUL}}$	mmHg · s^2/mL	0.000021	Pulmonary venous inertia
Parameters not used in the global sensitivity analysis	HR	s	80	Heart rate
	tC_{LA}	s	$0.75T_{\mathrm{HB}}$	Time of left atrial contraction
	TC_{LA}	s	$0.1T_{\mathrm{HB}}$	Duration of left atrial contraction
	tR_{LA}	s	$tC_{\mathrm{LA}} + TC_{\mathrm{LA}}$	Time of left atrial relaxation
	TR_{LA}	s	$0.8T_{\mathrm{HB}}$	Duration of left atrial relaxation
	tC_{LV}	s	0.0	Time of left ventricular contraction
	TC_{LV}	s	$0.265T_{\mathrm{HB}}$	Duration of left ventricular contraction
	tR_{LV}	s	$tC_{\mathrm{LV}} + TC_{\mathrm{LV}}$	Time of left ventricular relaxation
	TR_{LV}	s	$0.4T_{\mathrm{HB}}$	Duration of left ventricular relaxation
	tC_{RA}	s	$0.8T_{\mathrm{HB}}$	Time of right atrial contraction
	TC_{RA}	s	$0.1T_{\mathrm{HB}}$	Duration of right atrial contraction
	tR_{RA}	s	$tC_{\mathrm{RA}} + TC_{\mathrm{RA}}$	Time of left atrial relaxation
	TR_{RA}	s	$0.7T_{\mathrm{HB}}$	Duration of left atrial relaxation
	tC_{RV}	s	0.0	Time of right ventricular contraction
	TC_{RV}	s	$0.3T_{\mathrm{HB}}$	Duration of left ventricular contraction
	tR_{RV}	s	$tC_{\mathrm{RV}} + TC_{\mathrm{RV}}$	Time of right ventricular relaxation
	TR_{RV}	s	$0.4T_{\mathrm{HB}}$	Duration of left ventricular relaxation

The dynamics of the cardiac blood volumes account for both the inward and outward fluxes:

$$\dot{V}_{\mathrm{RA}}(t) = Q_{\mathrm{VEN}}^{\mathrm{SYS}}(t) - Q_{\mathrm{TV}}(t), \quad \dot{V}_{\mathrm{LA}}(t) = Q_{\mathrm{VEN}}^{\mathrm{PUL}}(t) - Q_{\mathrm{MV}}(t) \tag{2}$$

$$\dot{V}_{\mathrm{RV}}(t) = Q_{\mathrm{TV}}(t) - Q_{\mathrm{PV}}(t), \quad \dot{V}_{\mathrm{LV}}(t) = Q_{\mathrm{MV}}(t) - Q_{\mathrm{AV}}(t) \tag{3}$$

where $Q_{\mathrm{MV}}, Q_{\mathrm{AV}}, Q_{\mathrm{TV}}$ and Q_{PV} denote the blood flows through the mitral, aortic, tricuspid and pulmonary valves, respectively. These flows depend on the pressure jump between the upstream and downstream compartments:

$$Q_{\mathrm{TV}}(t) = Q_{\mathrm{valve}}(p_{\mathrm{RA}}(t) - p_{\mathrm{RV}}(t)), \quad Q_{\mathrm{MV}}(t) = Q_{\mathrm{valve}}(p_{\mathrm{LA}}(t) - p_{\mathrm{LV}}(t)) \tag{4}$$

$$Q_{\mathrm{PV}}(t) = Q_{\mathrm{valve}}(p_{\mathrm{RV}}(t) - p_{\mathrm{AR}}^{\mathrm{PUL}}(t)), \quad Q_{\mathrm{AV}}(t) = Q_{\mathrm{valve}}(p_{\mathrm{LV}}(t) - p_{\mathrm{AR}}^{\mathrm{SYS}}(t)) \tag{5}$$

where p_{LA}, p_{LV}, p_{RA} and p_{RV} are the unknown pressures inside the left atrium, left ventricle, right atrium, and right ventricle, respectively. The blood flow across each valve Q_{valve} is a function of the pressure jump across the valve:

$$Q_{\mathrm{valve}}(\Delta p) = \frac{\Delta p}{R_{\mathrm{valve}}(\Delta p)} \tag{6}$$

The resistance of the leaflets of each valve is:

$$R_{\mathrm{valve}}(\Delta p) = \sqrt{R_{\min} R_{\max}} \left(\frac{R_{\max}}{R_{\min}} \right)^{\frac{\operatorname{atan}(-100\pi\Delta p)}{\pi}} \tag{7}$$

R_{valve} ranges from $R_{\min}$ (open valve for $\Delta p \to +\infty$) to $R_{\max}$ (closed valve for $\Delta p \to -\infty$), where $R_{\min}$ and $R_{\max}$ are the minimal and maximal resistances imposed by the valve leaflets.

We model each cardiac chamber as a pressure generator. The pressure $p_{\mathrm{c}}(t)$ generated by the myocardium of the cardiac chamber c ($c \in \{LA, LV, RA, RV\}$) depends on the blood volume in the chamber $V_{\mathrm{c}}(t)$, the unloaded volume $V_{U,\mathrm{c}}$ (i.e., the volume at zero pressure) and the time-varying elastance $E_{\mathrm{c}}(t)$, which represents the contractility of the cardiac chamber.

$$p_{\mathrm{c}}(t) = E_{\mathrm{c}}(t)(V_{\mathrm{c}}(t) - V_{U,\mathrm{c}}) \tag{8}$$

The time-varying elastance $E_{\mathrm{c}}(t)$ depends on the passive elastance EB_{c} (i.e., the inverse of the chamber's compliance), the maximum active elastance EA_{c} and a periodic function $e_{\mathrm{c}}(t)$ that models the cardiac activation phases [3, 36].

$$E_{\mathrm{c}}(t) = EB_{\mathrm{c}} + EA_{\mathrm{c}} e_{\mathrm{c}}(t) \tag{9}$$

$$e_{\mathrm{c}}(t) = \begin{cases} \frac{1}{2}\left[1 - \cos\left(\frac{\pi}{TC_{\mathrm{c}}} \mathrm{mod}\left(t - tC_{\mathrm{c}}, T_{\mathrm{HB}}\right)\right)\right] \\ \quad \text{if } 0 \le \mathrm{mod}\left(t - tC_{\mathrm{c}}, T_{\mathrm{HB}}\right) < TC_{\mathrm{c}} \\ \frac{1}{2}\left[1 + \cos\left(\frac{\pi}{TR_{\mathrm{c}}} \mathrm{mod}\left(t - tR_{\mathrm{c}}, T_{\mathrm{HB}}\right)\right)\right] \\ \quad \text{if } 0 \le \mathrm{mod}\left(t - tR_{\mathrm{c}}, T_{\mathrm{HB}}\right) < TR_{\mathrm{c}} \\ 0 \quad \text{otherwise} \end{cases} \tag{10}$$

where TC_{c}, TR_{c}, tC_{c} and tR_{c} represent the durations of the contraction and relaxation phases and the times of the contraction and relaxation phases of the cardiac chamber, respectively (Table 1). The first and second equations in (10) correspond to the contraction and relaxation phases of the cardiac chamber, respectively.

Each circulatory compartment (e.g., systemic arterial circulation) is modeled as a Windkessel circuit (Figure 2), which describes the circulation using Kirchhoff's circuit laws. For instance, in the systemic arterial circulation:

$$L_{\mathrm{AR}}^{\mathrm{SYS}} \dot{Q}_{\mathrm{AR}}^{\mathrm{SYS}}(t) = -R_{\mathrm{AR}}^{\mathrm{SYS}} Q_{\mathrm{AR}}^{\mathrm{SYS}}(t) + p_{\mathrm{AR}}^{\mathrm{SYS}}(t) - p_{\mathrm{C}}^{\mathrm{SYS}}(t) \tag{11}$$

$$C_{\mathrm{AR}}^{\mathrm{SYS}} \dot{p}_{\mathrm{AR}}^{\mathrm{SYS}}(t) = Q_{\mathrm{AV}}(t) - Q_{\mathrm{AR}}^{\mathrm{SYS}}(t) \tag{12}$$

where $R_{\mathrm{AR}}^{\mathrm{SYS}}$, $C_{\mathrm{AR}}^{\mathrm{SYS}}$ and $L_{\mathrm{AR}}^{\mathrm{SYS}}$ represent the systemic arterial resistance, compliance, and inertia, respectively (Table 1). Similar equations apply to systemic venous circulation, pulmonary arterial circulation, and pulmonary venous circulation. For the capillary circulation the blood inertia is negligible [35], so we set it to 0, yielding:

$$R_{\mathrm{C}}^{\mathrm{SYS}} Q_{\mathrm{C}}^{\mathrm{SYS}}(t) = p_{\mathrm{C}}^{\mathrm{SYS}}(t) - p_{\mathrm{VEN}}^{\mathrm{SYS}}(t) \tag{13}$$

$$C_{\mathrm{C}}^{\mathrm{SYS}} \dot{p}_{\mathrm{C}}^{\mathrm{SYS}}(t) = Q_{\mathrm{AR}}^{\mathrm{SYS}}(t) - Q_{\mathrm{C}}^{\mathrm{SYS}}(t) \tag{14}$$

$$R_{\mathrm{C}}^{\mathrm{PUL}} Q_{\mathrm{C}}^{\mathrm{PUL}}(t) = p_{\mathrm{C}}^{\mathrm{PUL}}(t) - p_{\mathrm{VEN}}^{\mathrm{PUL}}(t) \tag{15}$$

$$R_{\mathrm{SH}} Q_{\mathrm{SH}}(t) = p_{\mathrm{C}}^{\mathrm{PUL}}(t) - p_{\mathrm{VEN}}^{\mathrm{PUL}}(t) \tag{16}$$

$$(C_{\mathrm{SH}} + C_{\mathrm{C}}^{\mathrm{PUL}}) \dot{p}_{\mathrm{C}}^{\mathrm{PUL}}(t) = Q_{\mathrm{AR}}^{\mathrm{PUL}}(t) - Q_{\mathrm{SH}}(t) - Q_{\mathrm{C}}^{\mathrm{PUL}}(t) \tag{17}$$

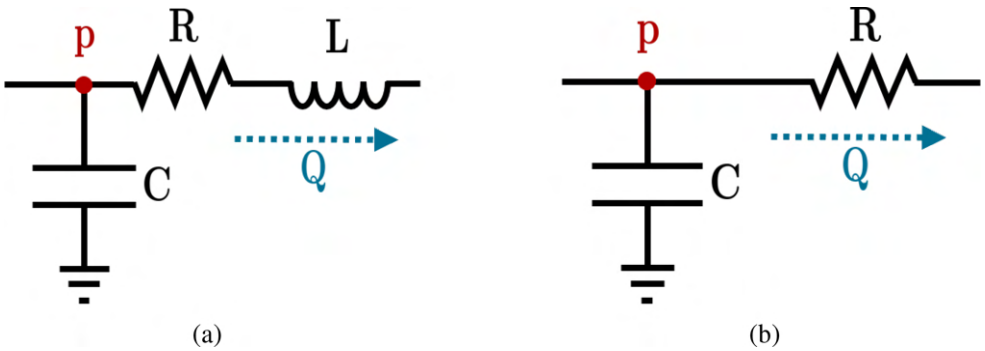

FIGURE 2 | RLC Windkessel circuit used for the arterial and venous compartments (a) and RC Windkessel circuit used for capillary compartments (b).

The first two equations refer to the systemic capillaries, where R_C^{SYS}, C_C^{SYS} and Q_C^{SYS} are the systemic capillary resistance, compliance and flux, respectively. The last three equations describe the pulmonary capillaries, where R_C^{PUL}, C_C^{PUL} and Q_C^{PUL} are the oxygenated pulmonary capillary resistance, compliance and flux, respectively, and R_{SH}, C_{SH} and Q_{SH} are the non-oxygenated resistance, compliance and flux, respectively. As shown in Equation (17), the two parallel compliances of the oxygenated and non-oxygenated compartments (Figure 1) act as a single equivalent compliance.

In summary, the entire dynamical system is:

$$\begin{cases} \dot{V}_{LA}(t) = Q_{VEN}^{PUL}(t) - Q_{MV}(t) \\ \dot{V}_{LV}(t) = Q_{MV}(t) - Q_{AV}(t) \\ C_{AR}^{SYS}\dot{p}_{AR}^{SYS}(t) = Q_{AV}(t) - Q_{AR}^{SYS}(t) \\ L_{AR}^{SYS}\dot{Q}_{AR}^{SYS}(t) = -R_{AR}^{SYS}Q_{AR}^{SYS}(t) + p_{AR}^{SYS}(t) - p_C^{SYS}(t) \\ C_C^{SYS}\dot{p}_C^{SYS}(t) = Q_{AR}^{SYS}(t) - Q_C^{SYS}(t) \\ C_{VEN}^{SYS}\dot{p}_{VEN}^{SYS}(t) = Q_C^{SYS}(t) - Q_{VEN}^{SYS}(t) \\ L_{VEN}^{SYS}\dot{Q}_{VEN}^{SYS}(t) = -R_{VEN}^{SYS}Q_{VEN}^{SYS}(t) + p_{VEN}^{SYS}(t) - p_{RA}(t) \\ \dot{V}_{RA}(t) = Q_{VEN}^{SYS}(t) - Q_{TV}(t) \\ \dot{V}_{RV}(t) = Q_{TV}(t) - Q_{PV}(t) \\ C_{AR}^{PUL}\dot{p}_{AR}^{PUL}(t) = Q_{PV}(t) - Q_{AR}^{PUL}(t) \\ L_{AR}^{PUL}\dot{Q}_{AR}^{PUL}(t) = -R_{AR}^{PUL}Q_{AR}^{PUL}(t) + p_{AR}^{PUL}(t) - p_C^{PUL}(t) \\ (C_{SH} + C_C^{PUL})\dot{p}_C^{PUL}(t) = Q_{AR}^{PUL}(t) - Q_{SH}(t) - Q_C^{PUL}(t) \\ C_{VEN}^{PUL}\dot{p}_{VEN}^{PUL}(t) = Q_{SH}(t) + Q_C^{PUL}(t) - Q_{VEN}^{PUL}(t) \\ L_{VEN}^{PUL}\dot{Q}_{VEN}^{PUL}(t) = -R_{VEN}^{PUL}Q_{VEN}^{PUL}(t) + p_{VEN}^{PUL}(t) - p_{LA}(t) \end{cases} \tag{18}$$

endowed with suitable initial conditions.

After discretizing the system and solving for the state variables, we calculate the model outputs $\mathbf{y}$. These model outputs, which are defined in Table 2, include indexed volumes, that is, normalized by the body surface area (BSA). The calibration procedure focuses on specific model outputs, in particular those in the upper section of Table 2.

We determine the reference setting of parameters $\mathbf{p}^R$ to reproduce an ideal healthy individual (see Table 1). Specifically, we fix HR = 80 bpm [34] and manually calibrate the other parameters as a modification of literature values [3, 35], so that the model outputs $\mathbf{y}$ align with echocardiographic ranges characteristic of a healthy individual (Table 2).

3 | Novel Calibration Methods

This section introduces the GSA along with the general aim of the calibration procedures (Section 3.1). The GSA is applied to all the calibration methods outlined in this study, reducing the number of parameters requiring calibration. We subsequently describe CMC in Section 3.2 and a hybrid method combining CMC and L-BFGS-B, referred to as CMC-L-BFGS-B, in Section 3.3.

3.1 | Global Sensitivity Analysis and Aim of the Calibration

We perform a global sensitivity analysis (GSA) to identify the parameters significantly affecting the model outputs used for calibration (Table 2). We compute the sensitivity of these model outputs to the parameters listed in Table 1. Due to the relatively small number of model outputs used for calibration (7) compared to the number of modifiable parameters (32), different parameter settings may yield similar model outputs. To address this issue and enhance structure identifiability, we select the most significant parameters for calibration, according to the GSA, while fixing the others. We do not compute the sensitivity to the HR, as it is easily measured from patients and therefore does not require calibration from indirect measures. Additionally, we excludes from the sensitivity analysis the timings of the cardiac cycle, as the pressure-volume (PV) loops of the cardiac chambers are highly sensitive to these parameters and their modification could result in non-physiological PV-loops.

For simplicity, we assume parameter independence and we let them vary randomly in a hypercube. Given the parameters independence, we estimate total Sobol' indices [24] to evaluate the impact of each parameter p_k on the variance of a certain model output y_j, accounting for both first-order and higher-order interactions among parameters:

$$S_k^{j,T} = 1 - \frac{Var_{\mathbf{p}_{\sim k}}[\mathbb{E}_{p_k}[y_j|\mathbf{p}_{\sim k}]]}{Var[y_j]} \tag{19}$$

where $\mathbf{p}_{\sim k}$ represents the set of all parameters except p_k. $\mathbb{E}$ and Var are the expected value and variance, respectively, and the subscripts indicate the random variable measure used for integration. When the subscript is absent, the integration is performed to all the random variables. $\mathbb{E}_{p_k}[y_j|\mathbf{p}_{\sim k}]$ is the expected value of the model output y_j conditioned with respect to the parameters $\mathbf{p}_{\sim k}$. We prefer total Sobol' indices over first-order ones because they account for both first and higher-order interactions between parameters, providing a more comprehensive understanding of the parameter influence on model output variability.

We use a Sobol' sequence [40] to sample parameters within the hypercube and we estimate the total Sobol' indices (19) using the Saltelli's method [41]. Sobol's sequences maximize the rate of convergence of the sample mean to the expected value of a distribution, reducing the computational costs of evaluating (19). We compute the model outputs corresponding to the sampled parameters using the lumped-parameter cardiocirculatory model. The parameter hypercube is centered around the reference setting of parameters $\mathbf{p}^R$ for a healthy individual (Appendix A). Saltelli's method allows for a linear increase in the number of samples to the number of parameters $N_p = 32$, resulting in $2N(N_p + 1)$ samples where N is a user-defined variable. For this analysis, we choose $N = 2^{12}$, leading to 270336 samples.

It is important to note that the shape and the position of the hypercube, where we sample the parameters, impact Sobol's indices. A wider range for a parameter results in higher Sobol indices, as it potentially increases the variability in the model outputs.

Based on the total Sobol' indices, we select $\hat{N}_p$ parameters for calibration. During the calibration procedure (which may be based on in silico data or patient-specific measurements), these parameters can vary within the ranges described in Appendix A. Although these ranges are fixed, they are sufficiently large to cover a wide variety of conditions.

TABLE 2 | List of model outputs, the units of measure, the echocardiographic ranges for a healthy individual and the values returned by the numerical model with the reference setting of parameters.

	Model output	Unit	Range	Model value	Description
Model outputs used for calibration	$LA_{\mathrm{I}-Vmax}$	mL/m^2	[16,34] [37]	22.2	Indexed maximal left atrial volume
	$LV_{\mathrm{I-EDV}}$	mL/m^2	[50,90] [38]	59.7	Indexed left ventricular end diastolic volume
	LV_{ESV}	mL	[18,52] [37]	42.7	Left ventricular end systolic volume
	LV_{EF}	%	[53,73] [37]	60.0	Left ventricular ejection fraction
	max ∇P_{rAV}	mmHg	—	17.4	Maximal right atrioventricular pressure gradient
	SAP_{max}	mmHg	[−, 140] [37]	109.6	Systolic systemic arterial pressure
	SAP_{min}	mmHg	[−, 80] [37]	71.3	Diastolic systemic arterial pressure
	PAP_{max}	mmHg	[15,28] [38]	23.6	Systolic pulmonary arterial pressure
Additional model outputs	LA_{Pmax}	mmHg	[6,20] [38]	10.3	Maximal left atrial pressure
	LA_{Pmin}	mmHg	[−2, 9] [38]	5.7	Minimal left atrial pressure
	LA_{Pmean}	mmHg	[4,12] [38]	8.8	Mean left atrial pressure
	LV_{SV}	mL	[30,80] [37]	64.1	Left ventricular stroke volume
	CI	L/min/m^2	[2.8,4.2] [38]	2.9	Cardiac index
	LV_{Pmax}	mmHg	[90,140] [38]	110.5	Maximal left ventricular pressure
	LV_{Pmin}	mmHg	[4,12] [38]	4.0	Minimal left ventricular pressure
	$RA_{\mathrm{I}-Vmax}$	mL/m^2	[10,36] [37]	29.3	Indexed maximal right atrial volume
	RA_{Pmax}	mmHg	[2,14] [38]	9.6	Maximal right atrial pressure
	RA_{Pmin}	mmHg	[−2, 6] [38]	4.4	Minimal right atrial pressure
	RA_{Pmean}	mmHg	[−1, 8] [38]	6.9	Mean right atrial pressure
	$RV_{\mathrm{I-EDV}}$	mL/m^2	[44,80] [39]	68.2	Indexed right ventricular end diastolic volume
	$RV_{\mathrm{I-ESV}}$	mL/m^2	[19,46] [39]	32.6	Indexed right ventricular end systolic volume
	RV_{EF}	%	[44,71] [39]	52.2	Right ventricular ejection fraction
	RV_{Pmax}	mmHg	[15,28] [38]	25.2	Maximal right ventricular pressure
	RV_{Pmin}	mmHg	[0,8] [38]	3.4	Minimal right ventricular pressure
	PAP_{min}	mmHg	[5,16] [38]	15.9	Diastolic pulmonary arterial pressure
	PAP_{mean}	mmHg	[10,22] [38]	19.5	Mean pulmonary arterial pressure
	PWP_{min}	mmHg	[1,12] [38]	11.5	Minimal pulmonary wedge pressure
	PWP_{mean}	mmHg	[6,15] [38]	12.0	Mean pulmonary wedge pressure
	SVR	mmHg · min/L	[11.3,17.5] [38]	16.2	Systemic vascular resistance
	PVR	mmHg · min/L	[1.9,3.1] [38]	2.09	Pulmonary vascular resistance
	Shunt fraction	%	[0,5] [31]	4.73	Shunt fraction

Given the large number of parameters analyzed (32) and the potentially high computational cost, a screening method, such as the Morris method [42], would generally be more appropriate for sensitivity analysis due to its reduced computational cost. However, in our case, Saltelli's method allows for a cost that scales linearly with the number of parameters. Additionally, the model simulations are not significantly expensive and parallel execution significantly reduces the overall computational time. Finally, thanks to the Sobol indices, we have an accurate variance description of the model outputs to the parameters.

The goal of calibration methods is to minimize the loss function (relative mean squared error):

$$rMSE(\mathbf{p}) = \frac{1}{N_{\mathrm{d}}} \sum_{\mathrm{i}=1}^{\mathrm{N_d}} \left(\frac{d_{\mathrm{i}} - y_{\mathrm{j(i)}}(\mathbf{p})}{d_{\mathrm{i}}} \right)^2 \tag{20}$$

where N_d is the number of available data d_i, for $1 \le i \le N_d$. Each data corresponds to a model output. The index $j(i)$ refers to the entry of the model outputs vector $\mathbf{y}$ approximating the ith data. $\mathbf{p}$ represents the parameter set.

3.2 | Correlation Matrix Calibration Method

CMC uses a surrogate for the gradient of the loss function. The Pearson correlation coefficient measures the linear relationship between two variables [43]. If $f : \mathbb{R} \to \mathbb{R}$ is a (non-constant) function such that $f(x) \le f(y)$ for almost every $x < y$ with $x, y \in \mathbb{R}$ drawn from an absolutely continuous distribution $X \sim g$, then the Pearson's correlation coefficient between X and $f(X)$ is non-negative:

$$\varrho_{X,f(X)} = \frac{\mathbb{E}[(X - \mathbb{E}[X])(f(X) - \mathbb{E}[f(X)])]}{\sqrt{\mathbb{E}[(X - \mathbb{E}[X])^2]\ \mathbb{E}[(f(X) - \mathbb{E}[f(X)])^2]}} \ge 0$$

Indeed, the numerator determines the sign of the correlation coefficient:

$$\begin{aligned}
&\mathbb{E}[(X - \mathbb{E}[X])(f(X) - \mathbb{E}[f(X)])] \\
&\quad = \mathbb{E}[(X - \mathbb{E}[X])(f(X) - f(\mathbb{E}[X]) + f(\mathbb{E}[X]) - \mathbb{E}[f(X)])] \\
&\quad = \mathbb{E}[(X - \mathbb{E}[X])(f(X) - f(\mathbb{E}[X]))] + (f(\mathbb{E}[X]) \\
&\qquad - \mathbb{E}[f(X)])\mathbb{E}[X - \mathbb{E}[X]] \\
&\quad = \mathbb{E}[(X - \mathbb{E}[X])(f(X) - f(\mathbb{E}[X]))] \\
&\quad = \int_{-\infty}^{+\infty} (x - \mathbb{E}[X])(f(x) - f(\mathbb{E}[X]))g(x)dx
\end{aligned}$$

Given the monotonicity of f almost everywhere, the signs of $x - \mathbb{E}[X]$ and $f(x) - f(\mathbb{E}[X])$ are concordant, ensuring that $\varrho_{X,f(X)} \ge 0$. The opposite is true if f is monotone non-increasing. For a set of n paired data points $\{(x_i, f(x_i))\}_{i=1}^n$ with $\overline{f(x)} = \frac{1}{n}\sum_{i=1}^n f(x_i)$, a similar argument applies to the sample Pearson's correlation coefficient [43] assuming f is monotone everywhere:

$$r_{X,f(X)} = \frac{\sum_{i=1}^n (x_i - \overline{x})(f(x_i) - \overline{f(x)})}{\sqrt{\left(\sum_{i=1}^n (x_i - \overline{x})^2\right)\left(\sum_{i=1}^n (f(x_i) - \overline{f(x)})^2\right)}} \ge 0$$

Thus, we leverage the sample correlation coefficient between model parameters and outputs to infer the monotonicity of the loss function and its gradient to the parameters.

To compute the correlation matrix M (where $M_{l,j} = r_{p_l,y_j}$), we perform $100\hat{N}_p$ tests, where $\hat{N}_p$ is the number of parameters selected by the GSA (Section 3.1). We sample the parameters from a uniform distribution within the previously defined hypercube and compute the corresponding model outputs. The correlation coefficients provide local information about the linear relationships between model parameters and outputs near the mean of the parameter distribution, which coincides with the hypercube's center due to the uniform sampling. Although CMC may lose accuracy when the parameter setting deviates from the hypercube's center during the calibration procedure, it still achieves good results for the cardiocirculatory model, as we show in Section 4.

ALGORITHM 1 | CMC algorithm.

1: Initialize: $\mathbf{d}$, tol, $it_{\max}$, $it = 0$, $m = \varnothing$
2: Load M
3: Choose the initial guess of parameters $\mathbf{p}$
4: **do**
5: Run a model simulation
6: $e_i = \frac{d_i - y_{j(i)}(\mathbf{p})}{d_i}$ for $i = 1, \dots, N_d$
7: Compute $\mathcal{L}(\mathbf{p})$
8: $\mathbf{a} = \mathbf{e}$
9: **if** $\mathcal{L}(\mathbf{p}) \ge tol$ **then**
10: **while** $\mathbf{a} \ne \mathbf{0}$ **do**
11: $par_{\text{con}} = 0$
12: $(\bar{\imath}, \bar{l}, \mathbf{a}, m, par_{\text{con}}) =$ choose_parameter $(M, \mathbf{a}, m, par_{\text{con}})$
13: **if** $m = \varnothing$ **then**
14: Go to line 10
15: **end if**
16: $\hat{\partial}\mathcal{L} =$ surrogate_gradient$(M, \mathbf{e}, \bar{\imath}, \bar{l})$
17: **if** $\hat{\partial}\mathcal{L} < 0$ **then**
18: $p_{\bar{l}} =$ calibrate$(\bar{l}, p_{\bar{l}}, p_{\bar{l}}^R, e_{\bar{\imath}}, M_{\bar{l},j(\bar{\imath})})$
19: $it = it + 1$
20: Break
21: **end if**
22: **end while**
23: **end if**
24: **while** $it \le it_{\max}$ & $\mathcal{L}(\mathbf{p}) \ge tol$ & $\mathbf{a} \ne \mathbf{0}$

The CMC algorithm (Algorithm 1) relies on three subroutines: *choose_parameter*, *surrogate_derivative* and *calibrate*, which will be explained later. The CMC algorithm for the cardiovascular system operates as follows:

1. Initialize variables (lines 1–3): $\mathbf{d}$, tol, $it_{\max}$, it, M, $\mathbf{p}$ and m. These represent the available data, calibration tolerance, maximum iterations, current iteration count, correlation matrix, initial parameter guess, and a set, respectively. The initial guess $\mathbf{p}$ lies within the hypercube used to build M. The initially empty set m stores the parameters considered (but not necessarily calibrated) during the calibration procedure. The *choose_parameter* subroutine handles this set to prevent favoring any single parameter during the calibration procedure.

2. Run a model simulation, compute the signed relative errors between data and model outputs, the loss function (20), and define an auxiliary vector $\mathbf{a}$ (lines 5–8). The error vector $\mathbf{e}$ is used to compute the surrogate derivative $\hat{\partial}\mathcal{L}$ in the *surrogate_derivative* subroutine and to determine how to modify a parameter in the *calibrate* subroutine. The auxiliary vector $\mathbf{a}$, along with M, m, par_{con} and $\hat{\partial}\mathcal{L}$, determines which parameter to calibrate and whether to continue the calibration procedure. The *choose_parameter* subroutine can set the components of $\mathbf{a}$ to 0. If all the components are 0, the while loop at line 10 is skipped and the calibration terminates as specified at line 24.

3. If the loss function exceeds the tolerance tol and while $\mathbf{a}$ is not a vector of 0s, define a variable $par_{\text{con}} = 0$ (lines 9–11). During the while loop (line 10) a specific error component $e_{\bar{\imath}}$ is selected for reduction and, accordingly, a parameter

$p_{\bar{l}}$ is chosen for calibration. The par_{con} variable tracks the number of parameters considered (but not necessarily calibrated) to reduce the selected error component $e_{\bar{i}}$. This allows us to determine if the set m was filled to reduce only the error $e_{\bar{i}}$ or also other error components, which affects the behavior of the *choose_parameter* subroutine.

4. Choose the parameter to calibrate (line 12). The *choose_parameter* subroutine updates **a**, m and par_{con}. Here, $\bar{i}$ is the index of the error component to reduce and $\bar{l}$ the index of the parameter to calibrate. Although the parameter $p_{\bar{l}}$ is selected for calibration, it might not be modified due to the conditional statement in line 17.

5. If, after running the *choose_parameter* subroutine, the set m is empty, return to line 10 (lines 13–15). This condition indicates that, at the current iteration of the while loop, no parameters outside of m before the execution of the *choose_parameter* subroutine were significant enough to reduce $e_{\bar{i}}$;

6. Surrogate the derivative of the loss function to $p_{\bar{l}}$ (line 16).

7. If the surrogate derivative of the loss function is negative, perform a calibration step, increment the iteration counter it, and repeat the procedure from step 2. If the derivative is not negative, go back to line 10 (lines 17–21). If a calibration step is performed, the model simulation is re-run to check whether the new parameter setting brings the loss function below the tolerance tol. Otherwise, the *choose_parameter* subroutine identifies another parameter to calibrate.

8. The calibration procedure stops when one of the following occurs: the maximum number of iterations is reached, the loss function falls below the prescribed tolerance or the vector **a** becomes **0** (line 24). The latter indicates that none of the relative errors can be further reduced using this calibration procedure.

The *choose_parameter* subroutine (Algorithm 2) takes as inputs the correlation matrix M between model parameters and outputs, the auxiliary vector **a**, the set m of parameters considered during the calibration procedure and the variable par_{con}, which tracks the parameters considered to reduce a specific error component. The outputs are the indices $\bar{i}$ and $\bar{l}$ of the error component to reduce and of the parameter selected for the calibration step, respectively, along with the updated **a**, m and par_{con}. The steps for the *choose_parameter* subroutine are as follows:

1. Compute $\bar{i}$, **b** and $\bar{l}$ (lines 1–3). $\bar{i}$ is the index of the error component with the maximum absolute value, **b** is the corresponding column of the correlation matrix and $\bar{l}$ is the index of the correlation coefficient with maximum absolute value in **b**. Since $e_{\bar{i}}$ is the maximum error in absolute value, we aim to reduce it. To select the parameter for modification, we choose the one that has the greatest effect on the model output at index $j(\bar{i})$ based on the correlation coefficients.

2. Check if the selected parameter $p_{\bar{l}}$ is in the set m and if its related correlation coefficient in absolute value $|b_{\bar{l}}|$ is greater than 0.05. If both conditions hold, discard the current parameter, set $b_{\bar{l}} = 0$, and select the next parameter by identifying the new maximum correlation coefficient in absolute value in **b** (lines 4–7). m stores the parameters used in the calibration procedure at a maximum of once. If a parameter in m is encountered a second time, it is skipped or m will be emptied. The while loop at line 4 ensures that the same parameter is not considered twice for the calibration. Additionally, the condition $|b_{\bar{l}}| > 0.05$ prevents the selection of parameters that do not significantly affect the model output $j(\bar{i})$.

3. Update m and par_{con} by inserting the new parameter index $\bar{l}$ into m and incrementing par_{con} by 1 (lines 8 and 9).

4. If $|b_{\bar{l}}| \leq 0.05$, check if the cardinality of the set m is equal to par_{con} (lines 10 and 11). This condition implies that the number of parameters considered for the calibration procedure matches the number considered to reduce the current error component. If this is the case, none of the parameters can reduce the current error component. The use of m ensures that the same parameters are not reused to reduce the loss function without exploring all possible options.

5. If the condition at line 11 holds, we set $a_{\bar{i}} = 0$ (lines 11–13). This indicates that, since the calibration of no parameter can significantly reduce the error $|e_{\bar{i}}|$, we no longer consider the reduction of $|e_{\bar{i}}|$.

6. Finally, if the condition at line 10 holds, set $par_{\text{con}} = 0$ and $m = \emptyset$ (lines 16 and 17) to restart the parameter count and to empty the set m.

ALGORITHM 2 | $(\bar{i}, \bar{l}, \mathbf{a}, m, par_{\text{con}}) =$ choose_parameter$(M, \mathbf{a}, m, par_{\text{con}})$.

1: $\bar{i} = \text{argmax}_{i=1,\ldots,N_d} |a_i|$
2: $\mathbf{b} = M_{:,j(\bar{i})}$
3: $\bar{l} = \text{argmax}_{l=1,\ldots,N_p} |b_l|$
4: **while** $\bar{l} \in m$ & $|b_{\bar{l}}| > 0.05$ **do**
5: $\quad b_{\bar{l}} = 0$
6: $\quad \bar{l} = \text{argmax}_{l=1,\ldots,N_p} |b_l|$
7: **end while**
8: $m = m \cup \{\bar{l}\}$
9: $par_{\text{con}} = par_{\text{con}} + 1$
10: **if** $|b_{\bar{l}}| \leq 0.05$ **then**
11: $\quad$ **if** $|m| = par_{\text{con}}$ **then**
12: $\quad\quad a_{\bar{i}} = 0$
13: $\quad$ **end if**
14: $\quad par_{\text{con}} = 0$
15: $\quad m = \varnothing$
16: **end if**

The *surrogate_derivative* subroutine (Algorithm 3) takes as inputs the correlation matrix M, the signed relative error vector **e** and the indices $\bar{i}$ and $\bar{l}$ representing the error component to reduce and the parameter selected for the calibration step, respectively. The output is the surrogate derivative $\hat{\partial}\mathcal{L}$ to $p_{\bar{l}}$ of the loss function. The steps for the *surrogate_derivative* subroutine are described as follows:

1. Initialize the surrogate derivative of the loss function to $p_{\bar{l}}$ to 0 (line 1).
2. Compute the surrogate derivative of the loss function by evaluating, for each model output related to the data, the

ALGORITHM 3 | $\hat{\partial}\mathcal{L} = \text{surrogate\_gradient}(M, \mathbf{e}, \bar{\imath}, \bar{l})$.

1: $\hat{\partial}\mathcal{L} = 0$
2: **for** $k = 1, \ldots, N_d$ **do**
3: **if** $e_{\bar{\imath}} M_{\bar{l},j(\bar{\imath})} e_k M_{\bar{l},j(k)} > 0$ **then**
4: **if** $|e_k| > 0.01$ **then**
5: $\hat{\partial}\mathcal{L} = \hat{\partial}\mathcal{L} - |M_{\bar{l},j(k)}|$
6: **end if**
7: **else**
8: $\hat{\partial}\mathcal{L} = \hat{\partial}\mathcal{L} + |M_{\bar{l},j(k)}|$
9: **end if**
10: **end for**

effect of modifying $p_{\bar{l}}$ (line 2–10). The $\bar{l}$th row of the correlation matrix stores the effect of modifying $p_{\bar{l}}$ on each model output. If, for $k = 1, \ldots, N_d$, e_k is greater than 0 then the $j(k)$th model output needs to increase to reduce the error. If $M_{\bar{l},j(k)}$ is greater than 0, increasing $p_{\bar{l}}$ increases the model output $j(k)$. Similar reasoning applies to other combinations of signs for e_k and $M_{\bar{l},j(k)}$. Consequently, if the sign of $e_k M_{\bar{l},j(k)}$ is positive or negative, then $p_{\bar{l}}$ has to increase or decrease, respectively, to reduce the error $|e_k|$. If the sign of $e_k M_{\bar{l},j(k)}$ matches the sign of $e_{\bar{\imath}} M_{\bar{l},j(\bar{\imath})}$, modifying $p_{\bar{l}}$ affects both e_k and $e_{\bar{\imath}}$ in the same way. Since, at the current calibration step, we aim to reduce $|e_{\bar{\imath}}|$, if modifying $p_{\bar{l}}$ according to $e_{\bar{\imath}} M_{\bar{l},j(\bar{\imath})}$ also reduces $|e_k|$, we add a negative value to the surrogate derivative of the loss function; otherwise, a positive value (lines 5 and 8). The impact of $p_{\bar{l}}$ on the model output $j(k)$ is measured by $|M_{\bar{l},j(\bar{\imath})}|$. The condition on line 4 ensures that, when e_k is nearly 0, its modification does not inadvertently increase the loss function.

Let $\bar{u}_{\bar{l}}$ and $\bar{b}_{\bar{l}}$ be the upper and lower bounds of the interval used to calibrate $p_{\bar{l}}$ (Appendix A). The *calibrate* subroutine updates $p_{\bar{l}}$ by sampling, at each iteration, from a uniform distribution over $(p_{\bar{l}}, \bar{u}_{\bar{l}})$ or $(\bar{b}_{\bar{l}}, p_{\bar{l}})$, depending on whether $e_{\bar{\imath}} M_{\bar{l},j(\bar{\imath})}$ is positive or negative, respectively. These bounds depend on $p_{\bar{l}}^R$ and the type of parameter being calibrated (e.g., $\bar{l}$ might refer to an active elastance). Due to the length of the code, we do not include the *calibrate* subroutine here.

CMC offers an advantageous trade-off between accuracy and complexity. Its gradient-free nature eliminates the need to compute gradients at each iteration of the calibration procedure, thereby reducing computational costs. However, since CMC relies on random steps, it may overlook local information, worsening the convergence. Due to this unpredictable random step, we force CMC to return the parameter setting achieving the lowest loss function.

3.3 | Hybrid Correlation Matrix Calibration-Limited Memory Broyden–Fletcher–Goldfarb–Shanno With Bound Constraints Method

The hybrid method CMC-L-BFGS-B initially applies CMC to avoid local minima associated with high loss function values and approach a better minimum. Subsequently, it applies L-BFGS-B [11] to refine this minimum estimate. L-BFGS-B is a quasi-Newton method designed to solve large non-linear optimization problems with simple bounds on the variables. The optimization problem is as follows:

$$\min f(\mathbf{x}) \text{ subjected to } l_i \leq x_i \leq u_i \text{ for } i = 1, \ldots, n \tag{21}$$

where $f : \mathbb{R}^n \to \mathbb{R}$ is a function with a known gradient ∇f, n is the dimension of the domain, $\mathbf{l}$ and $\mathbf{u}$ represent the lower and upper bounds for each variable. L-BFGS-B solves (21) by minimizing at each iteration the quadratic approximation of f:

$$m_k(\mathbf{x}) := f(\mathbf{x}_k) + \nabla f(\mathbf{x}_k)^T(\mathbf{x} - \mathbf{x}_k) + \frac{1}{2}(\mathbf{x} - \mathbf{x}_k)^T B_k(\mathbf{x} - \mathbf{x}_k) \tag{22}$$

where $\mathbf{x} \in \mathbb{R}^n$ is subjected to the bounds $\mathbf{l}$ and $\mathbf{u}$, $\mathbf{x}_k$ is the approximate solution at iteration k and B_k is a limited memory approximation of the Hessian matrix of f, obtained using the last $m \leq k$ approximate solutions and their corresponding gradient evaluations.

4 | Results

This section presents the results of the following tests for CMC, L-BFGS-B, and CMC-L-BFGS-B:

1. Robustness to in silico-generated data (Section 4.1).
2. Robustness to the initial guess of parameters (Section 4.2).
3. Robustness with respect to noisy data (Section 4.3).
4. Calibration based on patient-specific data (Section 4.4).
5. Effects of fixed steps in CMC (Section 4.5).

To validate CMC and CMC-L-BFGS-B, we show that these calibration techniques achieve results comparable to L-BFGS-B.

For tests 1, 2, 3, 5, we build a dataset of in silico-generated data, referred to as *virtual patients* or *samples*. We initially identified the parameters to calibrate by performing the GSA over the ranges not associated with COVID-19 pneumonia (Appendix A). We consider the Sobol' index estimates to be converged when, as in this case, all the confidence interval widths are less than 0.1 (Figure 3). Moreover, for dataset generation, correlation matrix computation, and calibration, we select parameters with at least one Sobol' index greater than 0.1 (Figure 4), namely: EB_{LA}, EA_{LV}, EB_{LV}, EB_{RV}, R_{AR}^{SYS}, C_{AR}^{SYS} and R_{VEN}^{SYS}. We generate the dataset by sampling these parameters from a uniform distribution over the ranges not associated with COVID-19 pneumonia (Appendix A) and computing the related model outputs. Note that, during the calibration procedure, the sum of C_C^{PUL} and C_{SH} in the dynamical system (16) may lead to instabilities, as different parameter values could yield the same equivalent compliance. However, the GSA results prevent this issue, as these two parameters are fixed. Since there are 7 parameters to calibrate, we estimate the correlation matrix by performing $100 \cdot 7 = 700$ tests, as stated in Section 3.2.

For test 4, we proceed analogously but we use the ranges associated with COVID-19 pneumonia for the GSA, the correlation matrix computation, and the calibration procedures.

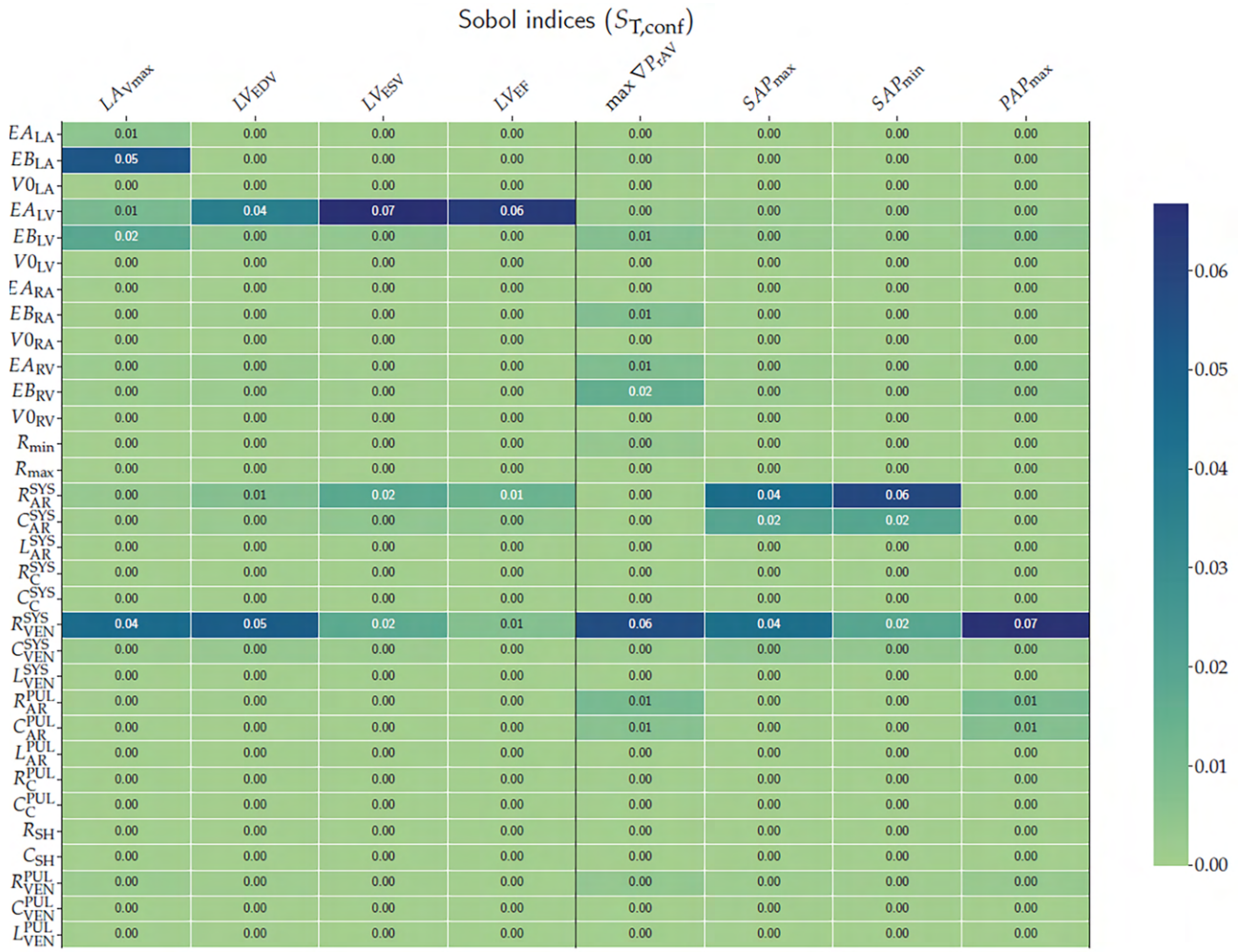

FIGURE 3 | Confidence intervals widths of the total-effect Sobol' indices between model parameters and outputs used for the calibration. A detailed definition of model parameters and outputs is provided in Tables 1 and 2.

We implement CMC in Matlab and L-BFGS-B in Python. We compute the numerical solution of the lumped-parameter cardiocirculatory model, in Matlab, by means of *ode15s* solver, a variable step and variable order solver, whereas, in Python, by means of the Dormand-Prince method, an adaptive stepsize Runge-Kutta method.

For each parameter setting, we run the model for 25 cycles until convergence to the regime solution of the dynamical system. To verify that 25 cycles are sufficient for convergence, one can evaluate the relative distance between the state variables in the last and second to last heartbeat. Since the state variables $\mathbf{x}(t)$ are $C^1[0, T]$, we compute the weighted relative distance:

$$\max_{i=1,\dots,n_{states}} \frac{\|x_i(t) - x_i(t - T_{HB})\|_{C^1(I),h}}{\|x_i(t)\|_{C^1(I),h}} = \tag{23}$$

$$\max_{i=1,\dots,n_{states}} \frac{\|x_i(t) - x_i(t - T_{HB})\|_{C^0(I)} + h\left|x_i(t) - x_i(t - T_{HB})\right|_{C^1(I)}}{\|x_i(t)\|_{C^0(I)} + h\left|x_i(t)\right|_{C^1(I)}} \tag{24}$$

where n_{states} is the number of dynamical system states (18), $I \subseteq [T_{HB}, 25T_{HB}]$ is an interval, $\|\cdot\|_{C^0(I)}$ and $|\cdot|_{C^1(I)}$ are the infinite norms of a function and its derivative over I, respectively, and h is the mesh size used for the discretization. A simulation using the reference parameter setting $\mathbf{p}^R$ (Table 1), for $I = [24T_{HB}, 25T_{HB}]$ yields a weighted relative distance of order 10^{-4}, indicating a small discrepancy on the states between successive heartbeats. Notably, $\mathbf{p}^R$ is not a favorable setting to analyze, as for $I = [T_{HB}, 2T_{HB}]$ the weighted relative distance is equal to 1.4. For the subsequent analysis, we only consider the last heartbeat.

The use of different software libraries (Matlab and Python) to implement the algorithms does not introduce significant biases. Indeed, in Section 4.1, we compare the performances of the calibration methods in terms of the number of evaluations of the loss function and its gradient, which does not depend on the implementation. Furthermore, the computational time of a single Matlab or Python numerical simulation is around 2.5 s (on a laptop with 12th Gen Intel(R) Core(TM) i7-12650 H, 2.30 GHz, 16 GB RAM).

For L-BFGS-B, we compute the exact gradient of the loss function by means of automatic differentiation. Since we are considering a loss function $\mathcal{L} : \mathbb{R}^{N_p} \to \mathbb{R}$ where $N_p \geq 1$, it is more efficient to use reverse (rather than forward) mode automatic differentiation, as it allows the computation of the gradient in a single iteration rather than N_p iterations. To compute the reverse mode gradient,

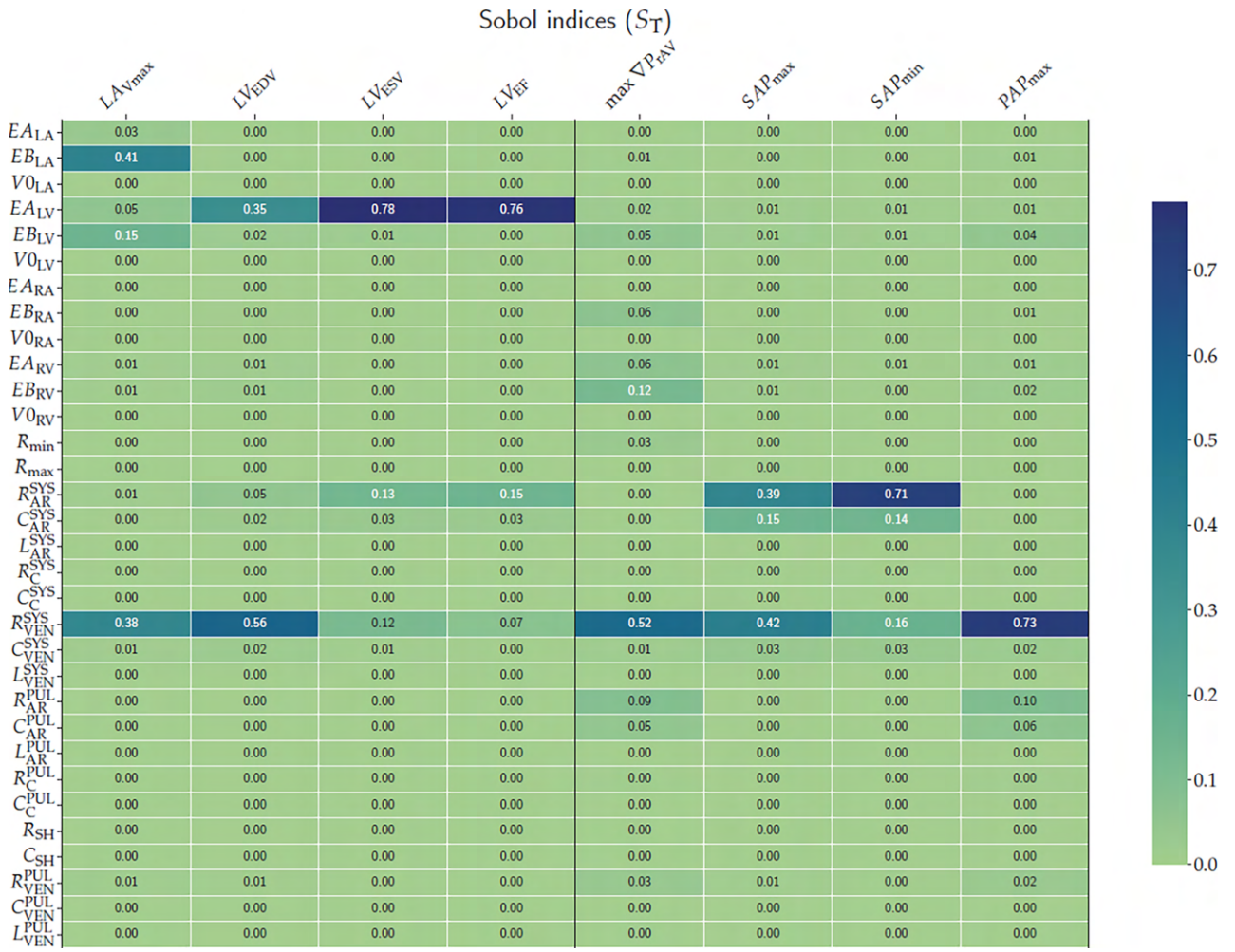

FIGURE 4 | Total-effect Sobol' indices between model parameters and outputs used for the calibration. A detailed definition of model parameters and outputs is provided in Tables 1 and 2.

TABLE 3 | Expected measurement errors, derived from the device sensitivity, on the model outputs and used as standard deviations for generating the noisy data.

LA_{Vmax}	LV_{EDV}	LV_{ESV}	LV_{EF}	$\max \nabla P_{\mathrm{rAV}}$	SAP_{max}	SAP_{min}	PAP_{max}
5%	5%	5%	4%	4%	4%	5%	5%

we use the Python library *Jax* [44, 45]. Once the gradient is available, we apply L-BFGS-B to minimize the loss function.

We consider a calibration procedure successful if the relative root mean squared error

$$rRMSE(\mathbf{p}) = \sqrt{rMSE(\mathbf{p})} \tag{25}$$

falls below 10^{-1}. This criterion demands less precision than the expected measurement errors, derived from the device sensitivity, in the model outputs used for calibration (Table 3), thereby avoiding that the minimization is targeting solely the data noise. Moreover, this condition is not loose, still allowing for effective calibration. Even when this condition is met, each calibration method continues to seek more accurate parameter estimates. CMC terminates after 500 iterations, achieving an $rMSE$ lower than 10^{-8} or getting stuck to a parameter set for which, according to Algorithm 1, $\mathbf{a} = \mathbf{0}$ without modifying any parameters. Instead, L-BFGS-B stops after 500 iterations, when the relative difference in the $rMSE$ between two successive iterations is less than 10^{-10} or when the infinite norm of the projected gradient of the $rMSE$ is less than 10^{-10}. CMC-L-BFGS-B first performs some steps of CMC to obtain an $rMSE$ lower than $2.5 \cdot 10^{-2}$, then it applies L-BFGS-B, which stops according to the same criteria as above.

4.1 | Test 1: Robustness and Accuracy on Silico-Generated Data

In this section, we evaluate the robustness of the calibration methods in estimating parameters on a dataset of 20 different in silico-generated patients (Table 4). Note that we do not estimate HR, as it is easily measured from patients and we use it as an input. The initial parameter setting for the calibration procedures is displayed in Table 1.

TABLE 4 | Parameters of 20 in silico-generated virtual patients.

Patient	HR	EB_{LA}	EA_{LV}	EB_{LV}	EB_{RV}	R_{AR}^{SYS}	C_{AR}^{SYS}	R_{VEN}^{SYS}
1	81	0.38	4.16	0.03	0.06	0.70	0.62	0.25
2	65	0.43	4.37	0.04	0.07	0.95	1.31	0.50
3	97	0.24	4.20	0.10	0.07	0.71	0.51	0.53
4	61	0.33	3.63	0.09	0.04	0.71	0.75	0.46
5	61	0.19	1.07	0.03	0.06	0.74	1.01	0.58
6	85	0.25	2.27	0.09	0.06	0.34	1.31	0.33
7	79	0.35	3.62	0.05	0.05	0.71	0.73	0.18
8	87	0.44	2.13	0.08	0.03	0.79	0.90	0.36
9	70	0.41	4.35	0.07	0.02	0.31	0.90	0.52
10	78	0.38	1.78	0.11	0.03	0.35	0.89	0.42
11	90	0.22	3.89	0.08	0.04	0.92	0.95	0.48
12	65	0.23	2.94	0.03	0.02	0.62	1.83	0.57
13	81	0.29	2.59	0.02	0.03	0.32	1.85	0.27
14	63	0.15	3.07	0.05	0.05	0.74	1.77	0.34
15	77	0.17	4.19	0.04	0.06	0.62	2.21	0.16
16	75	0.13	4.36	0.02	0.06	0.84	1.99	0.16
17	65	0.18	3.78	0.06	0.06	0.34	0.91	0.19
18	80	0.40	2.99	0.07	0.02	0.87	1.55	0.29
19	61	0.23	1.17	0.05	0.02	0.34	0.87	0.32
20	64	0.41	4.30	0.07	0.04	0.46	2.04	0.30

CMC is successful for 20 samples, while L-BFGS-B is successful for 18 samples and CMC-L-BFGS-B for 20 samples (Figure 5a), mirroring the performance of CMC. This suggests that the CMC step provides a good initial guess for L-BFGS-B. Figure 6 shows that CMC tends to be biased when estimating LV_{ESV} and, consequently, LV_{EF} as the confidence intervals for the mean difference between real and estimated model outputs almost exclude 0. Furthermore, the confidence intervals for the mean difference between real and estimated model outputs obtained with CMC-L-BFGS-B are narrower than those obtained with CMC alone, indicating that the L-BFGS-B step improves the model output estimates of CMC.

Despite CMC's higher number of successful calibrations, L-BFGS-B estimates parameters more precisely, achieving a lower overall $rRMSE$ than CMC (Figure 5b). CMC-L-BFGS-B exhibits similar behavior to L-BFGS-B. Nonetheless, CMC achieves similar $rRMSE$ across all samples. Analyzing the scatter plots between real and estimated parameters (Figure 7a), we observe that, for CMC, the points are more scattered compared to the other two methods, suggesting that CMC's higher calibration success rate than L-BFGS-B comes at the cost of a less accurate parameter estimation. This observation is further supported by the Bland-Altman plot comparing real and estimated parameters (Figure 7b), where CMC shows significantly larger confidence intervals of the mean difference between real and estimated parameters for EB_{LA}, EB_{LV} and R_{VEN}^{SYS} compared to L-BFGS-B. This also reflected in CMC-L-BFGS-B, indicating that the initial guess provided by CMC can affect the precision of L-BFGS-B estimates.

Finally, we evaluate the computational time and the number of evaluations of the loss function and its gradient for the three calibration methods (Table 5) on a standard laptop (12th Gen Intel(R) Core(TM) i7-12650H, 2.30 GHz, 16GB RAM). CMC is more than 3 times faster than L-BFGS-B in terms of computational time. Instead, CMC-L-BFGS-B is slower than L-BFGS-B because the CMC step's initial guess increases the computational time for the subsequent L-BFGS-B step. The average number of loss function evaluations for CMC matches the maximum number of iterations (500), meaning that the stopping criterion $\mathbf{a} = \mathbf{0}$ never occurs. Nonetheless, CMC typically achieves the minimum loss in less than 500 function evaluations (on average 243), suggesting that a more refined stopping criterion could improve CMC's performance. L-BFGS-B and CMC-L-BFGS-B are slower than CMC because computing the gradient of the loss function is more computationally demanding than evaluating the loss function itself. Both CMC and CMC-L-BFGS-B require the computation of the correlation matrix between model parameters and outputs, that slightly impacts the total computational time of these methods.

4.2 | Test 2: Robustness With Respect to the Initial Guess of Parameters

In this section, we test the robustness of the calibration methods on patient nine of Table 4 to the initial guess of parameters. We chose sample 9 because all the calibration methods achieved a successful calibration for this sample (Figure 5). Moreover, selecting a sample with *rRMSE* close to 0 for certain methods could result in different initial guesses leading to the same parameter estimate. While this demonstrates the robustness of the initial

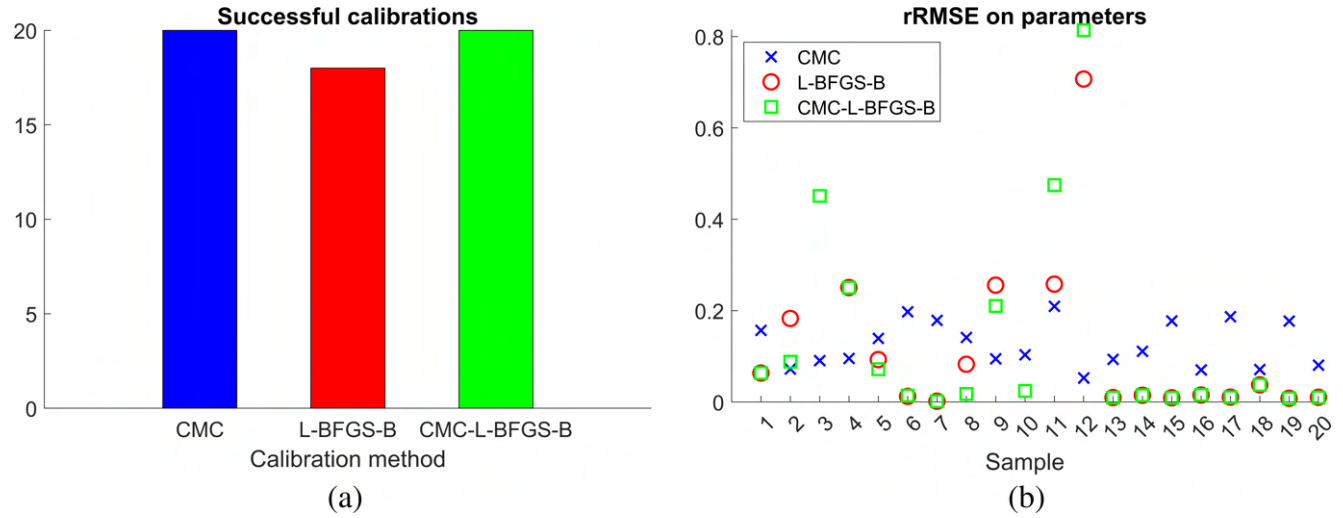

FIGURE 5 | Test 1. Number of successful calibration procedures for each calibration method (a) and *rRMSE* between estimated and real parameters for each sample (b). Only successful calibrations are reported.

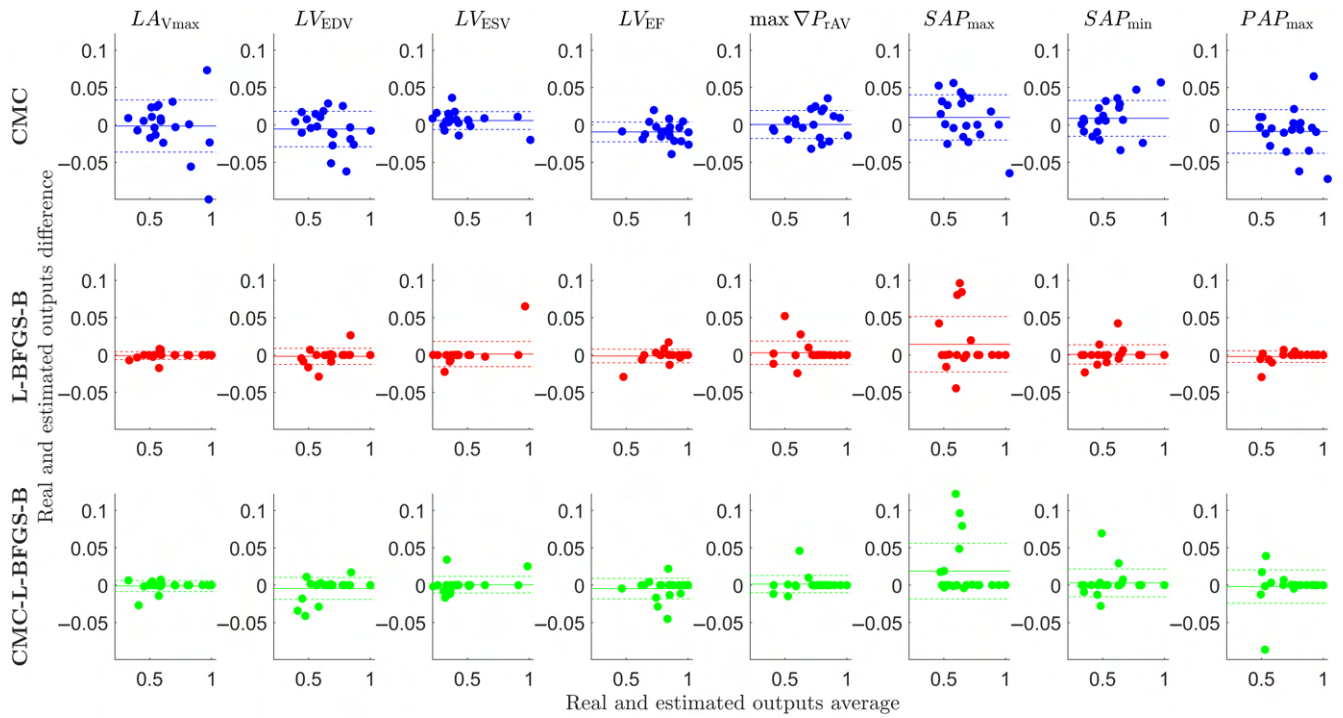

FIGURE 6 | Test 1. Bland-Altman plots between normalized real and estimated model outputs. We represent by means of continuous lines the mean of the difference between real and estimated model outputs, and with the dashed lines the 95% confidence interval for this mean. Each model output is normalized with respect to its maximum value across the 20 in silico-generated data. Only successful calibrations are reported.

parameter guess, we aim to stress each method with a less favorable sample, which is why we chose sample 9 for this test. We initiated the calibration procedures from 20 different randomly selected initial parameter settings, each within the associated ranges for the calibration procedure. Our goal is to determine if the three calibration methods would converge to the same parameter setting.

As preliminary results, CMC successfully calibrates the model for all 20 initial settings, while L-BFGS-B succeeds for 16 settings and CMC-L-BFGS-B for 20 settings (Figure 8a). CMC is more robust in estimating the model outputs than the other two methods, as the box plots for the difference between real and estimated outputs are smaller (Figure 9). Moreover, L-BFGS-B and CMC-L-BFGS-B produce biased estimates of $\max \nabla P_{\mathrm{rAV}}$, SAP_{max} and SAP_{min} with respect to their actual value.

Unlike the previous section, CMC achieves smaller parameter errors compared to the other two methods (Figure 8b). To further evaluate the robustness of the calibration methods, we calculate the relative standard deviation of each estimated parameter to its true value (Figure 8c). High relative standard deviations indicate different parameter estimates across different samples.

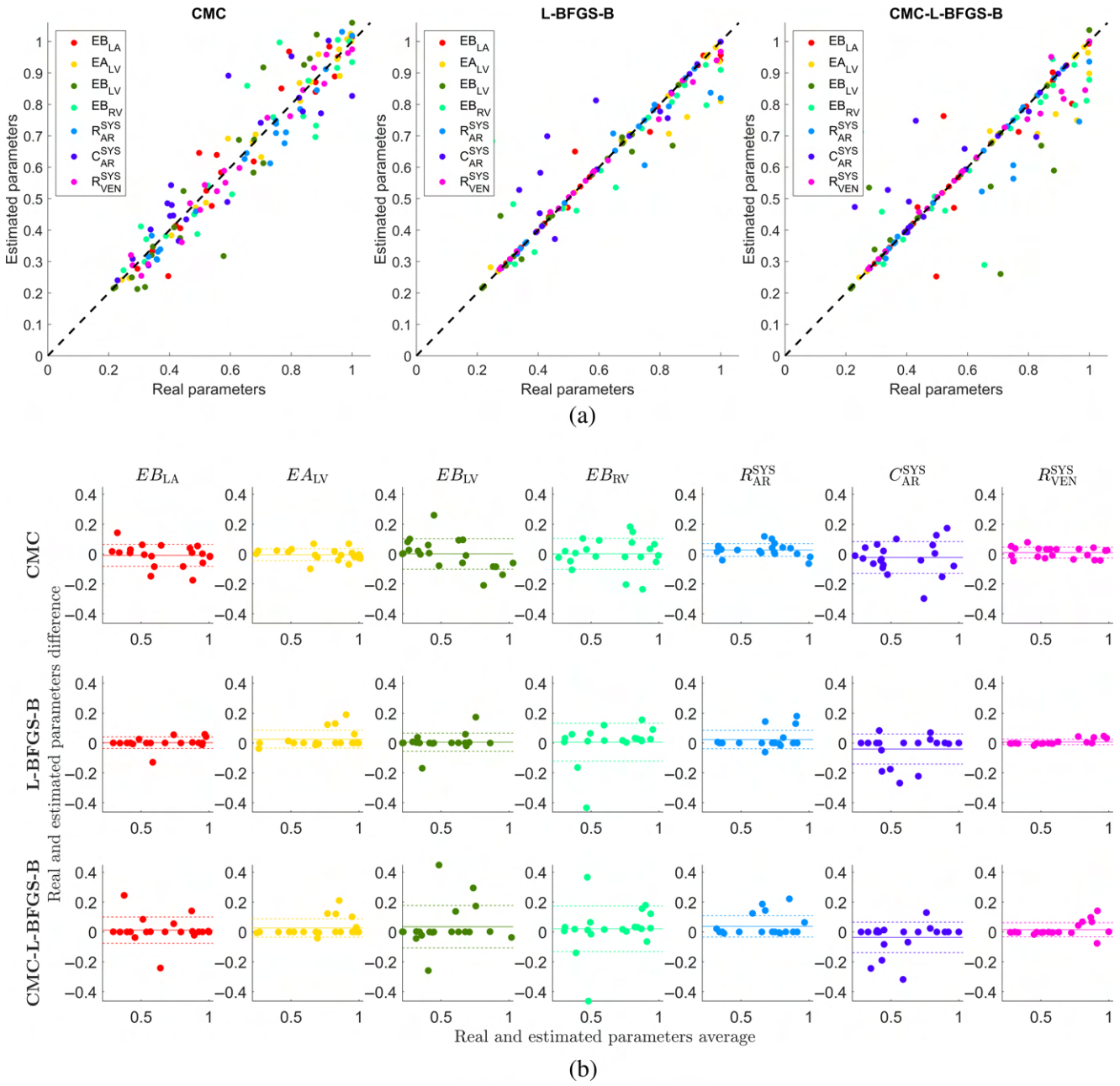

FIGURE 7 | Test 1. (a) Scatter plots between normalized real and estimated parameters. (b) Bland-Altman plots between normalized real and estimated parameters. With the continuous lines, we represent the mean of the difference between real and estimated parameters, and with the dashed lines the 95% confidence interval for this mean. Each parameter is normalized with respect to its maximum value across the 20 in silico-generated data. For both figures, only successful calibrations are reported.

TABLE 5 | Test 1. Total and average computational times of the three calibration methods along with the average loss function and gradient of the loss function evaluations. The average is computed across the 20 in silico-generated data. CMC does not use the gradient of the loss function. Computational time and number of model simulations run to compute the correlation matrix between model parameters and outputs.

	Average time [min]	Total time [h]	Average loss evaluations	Average gradient loss evaluations
CMC	16.9	6.0	500	—
L-BFGS-B	57.6	19.2	120	120
CMC-L-BFGS-B	66.0	22.4	146	142
	Total time		Number of model simulations	
Correlation matrix estimate	24.1 min		700	

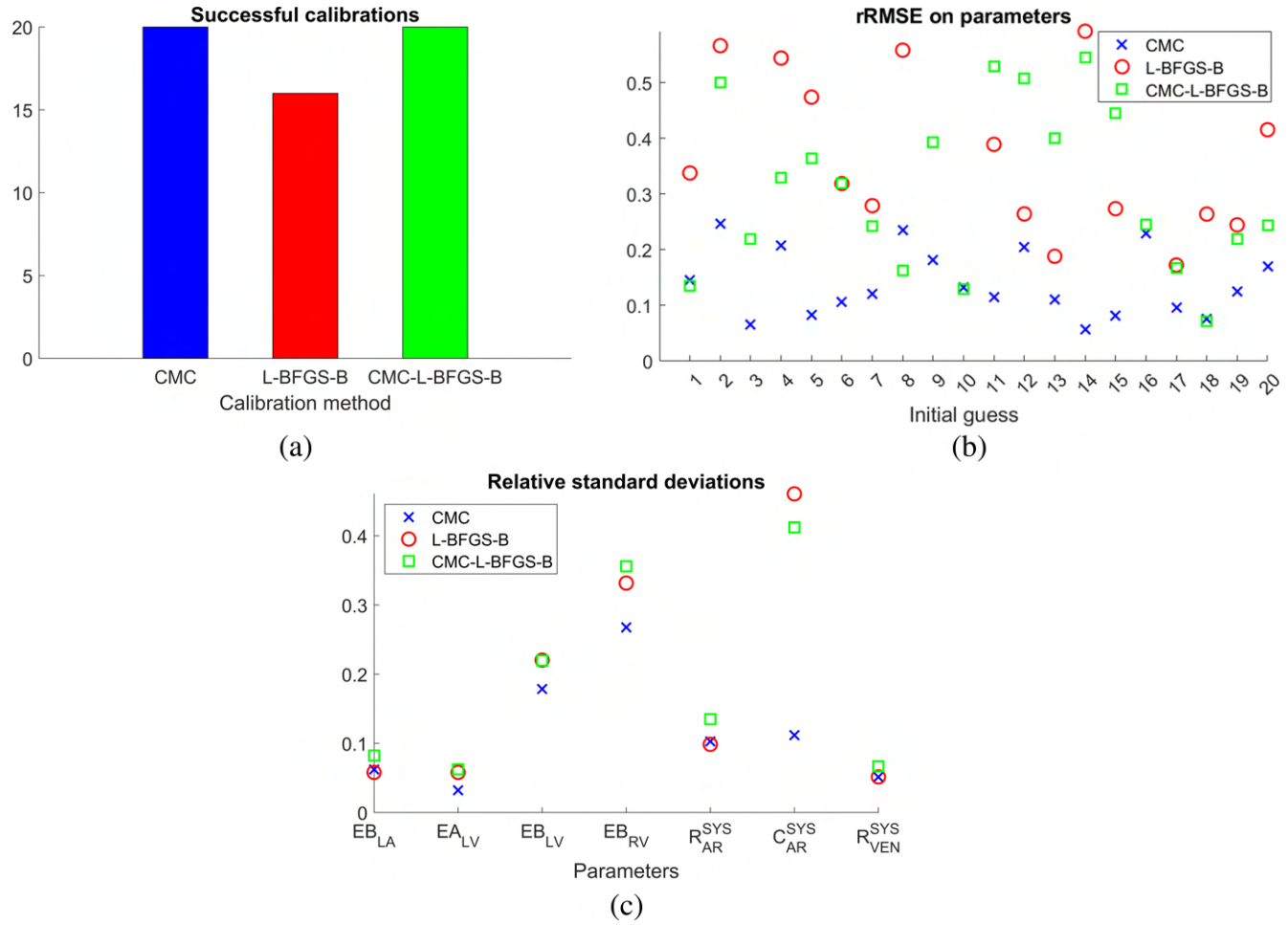

FIGURE 8 | Test 2. Number of successful calibration procedures for each calibration method (a), *rRMSE* between estimated and real parameters for each initial guess of parameters (b) and relative standard deviations of the estimated parameters (c). Only successful calibrations are reported.

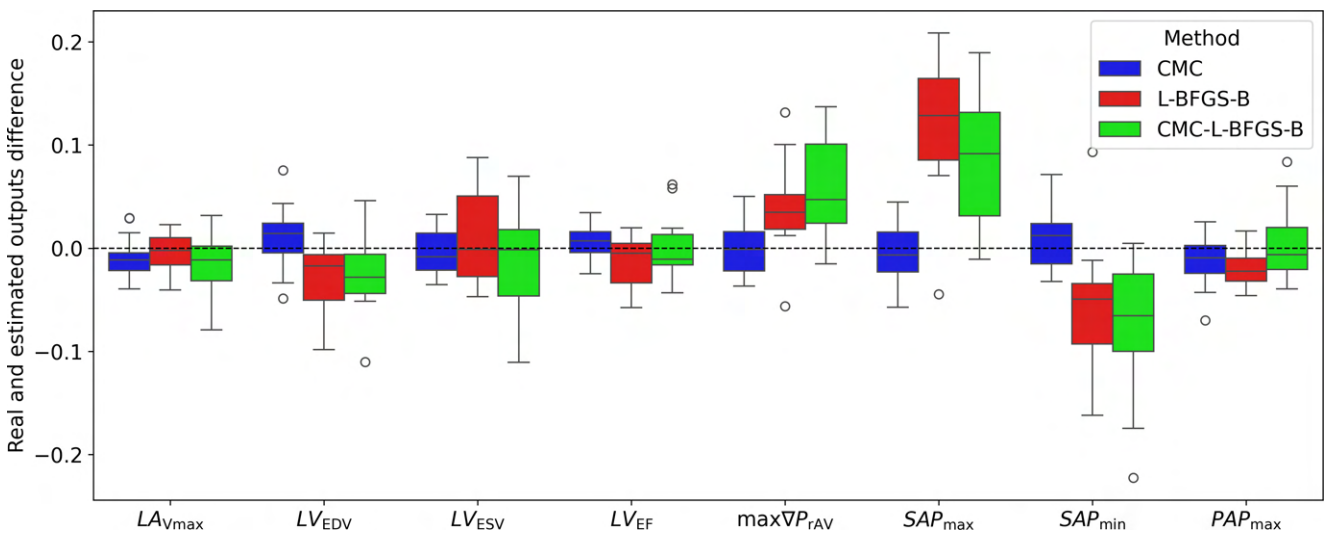

FIGURE 9 | Test 2. Box plots of the normalized real and estimated model outputs difference. We represent the zero difference with a dashed line, indicating perfect accuracy in prediction. Each model output is normalized with respect to its value of the in silico patient nine. Only successful calibrations are reported.

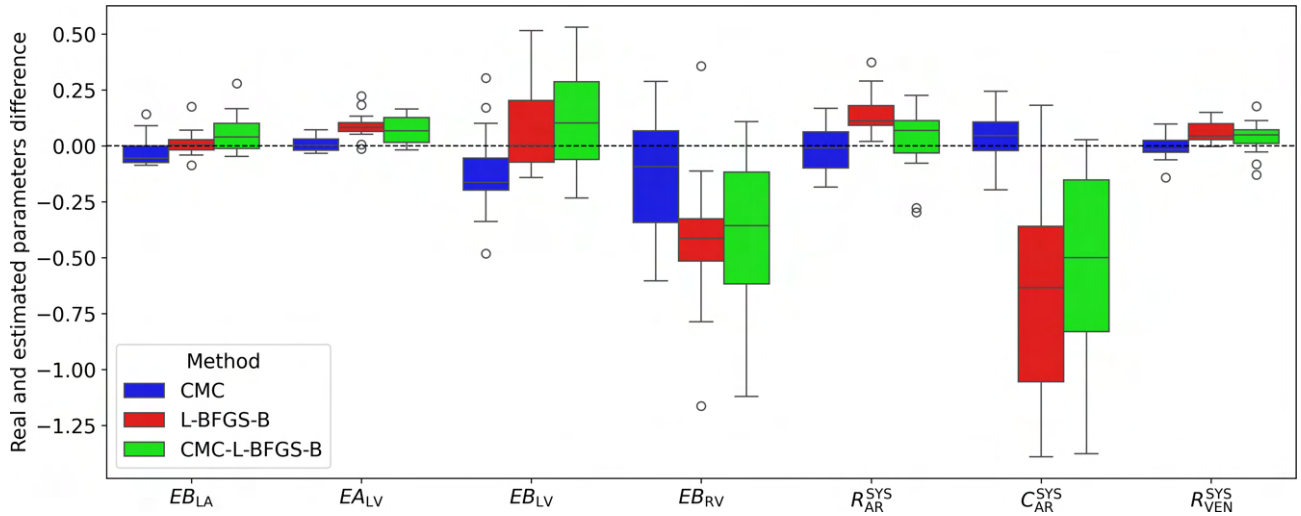

FIGURE 10 | Test 2. Box plots of the normalized real and estimated parameters difference. We represent the zero difference with a dashed line, indicating perfect accuracy in prediction. Each parameter is normalized with respect to its value of the in silico patient nine. Only successful calibrations are reported.

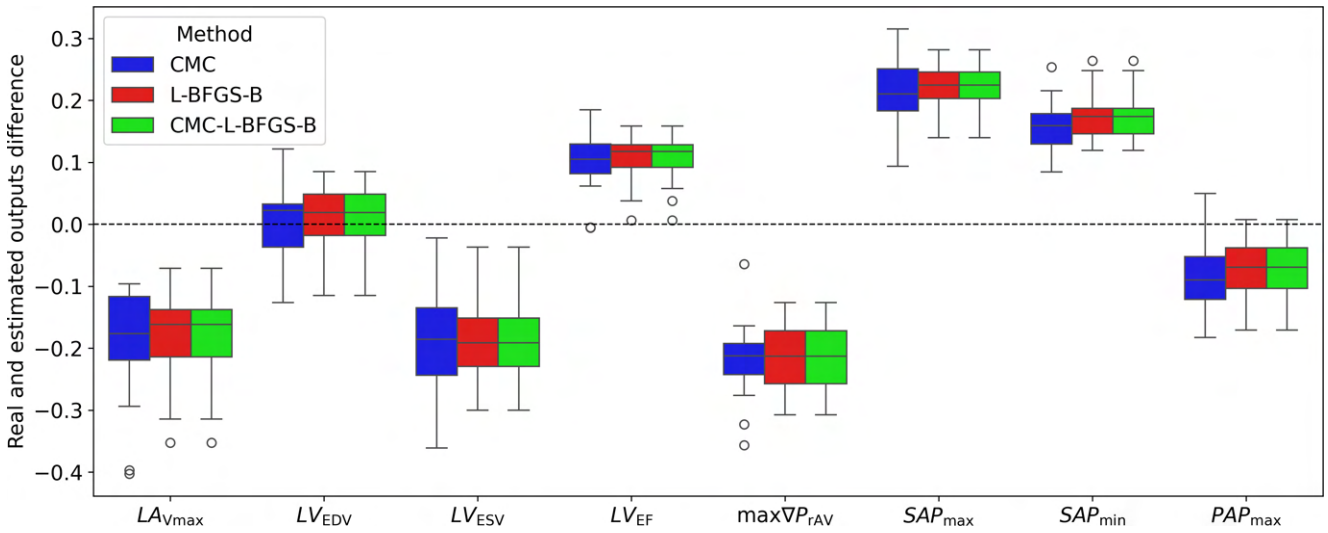

FIGURE 11 | Test 3. Box plots of normalized real and estimated model outputs difference. We represent the zero difference with a dashed line, indicating perfect accuracy in prediction. Each model output is normalized with respect to its value of the in silico patient seven. Only successful calibrations are reported.

Except for C_{AR}^{SYS}, where CMC exhibits the lowest relative standard deviation, the three methods follow a similar trend, indicating similar robustness to the initial parameter guess. From the box plots of the difference between real and estimated parameters (Figure 10), we observe that CMC estimates the parameters more precisely than the other two methods. Moreover, L-BFGS-B and CMC-L-BFGS-B poorly estimate EB_{RV} and C_{AR}^{SYS}, that affect significantly the estimates of max ∇P_{rAV}, SAP_{max} and SAP_{min}.

4.3 | Test 3: Robustness With Eespect to Noisy Data

In this section, we introduce synthetic noise to patient seven of Table 4, generating a dataset of 20 samples. Noisy data represent a realistic scenario, making the ability to accurately estimate the parameters under this condition critical for calibration methods. We sample the noise of each data from a normal distribution with zero mean and standard deviation equal to the expected measurement error associated with the data (Table 3). The initial parameter setting for the calibration procedures is displayed in Table 1.

All three calibration methods successfully calibrated the model for all 20 samples. However, the model output estimates for all three methods are biased to the real values, with CMC producing slightly larger box plots (Figure 11). This bias is a consequence of the noise in the data, even though the three methods estimate similar model outputs. Computing the *rRMSE* between model outputs and actual data (without noise), we obtain, for all the samples, higher errors than the *rRMSE* computed to noisy data (Figure 12a in the case of CMC).

As in Section 4.2, the three methods exhibit similar trends in the relative standard deviations (Figure 12b), indicating comparable

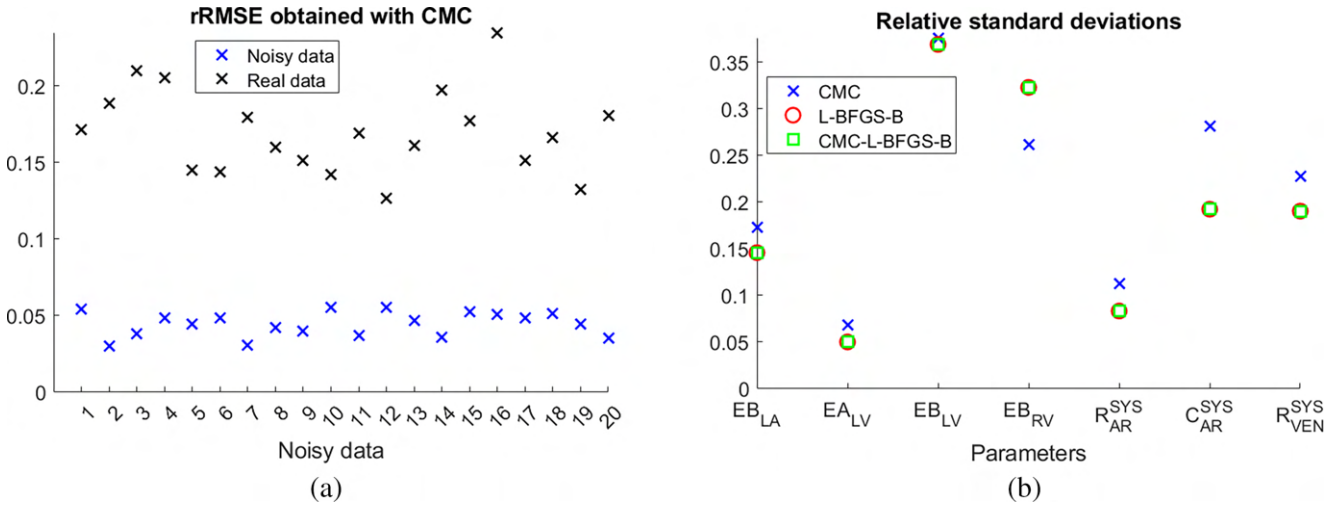

FIGURE 12 | Test 3. $rRMSE$ on noisy and actual in silico-generated data for CMC (a) and relative standard deviations of the estimated parameters for the 20 samples (b).

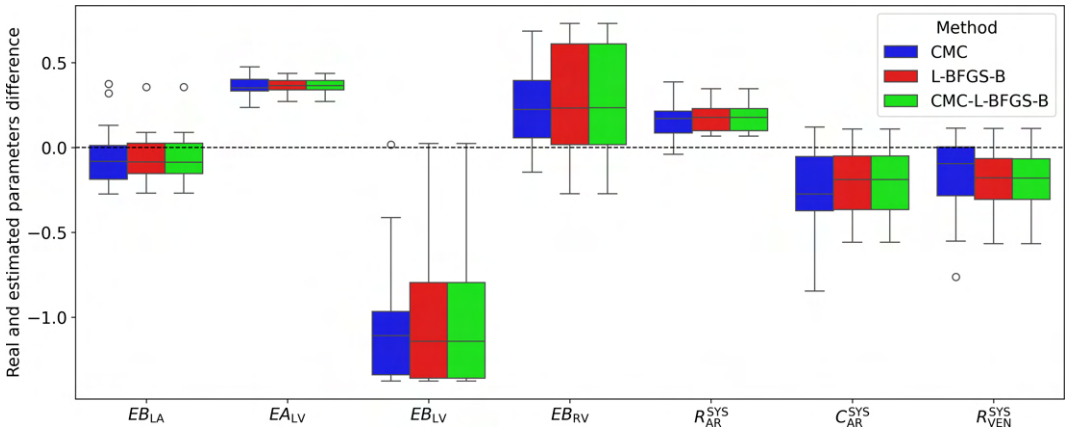

FIGURE 13 | Test 3. Box plots of normalized real and estimated parameters difference. We represent the zero difference with a dashed line, indicating perfect accuracy in prediction. Each parameter is normalized with respect to its value of the in silico patient seven. Only successful calibrations are reported.

robustness to noisy data. In terms of parameter estimates, the three calibration methods perform similarly (Figure 13). Even if for EB_{LV} and EB_{RV} the box plots for CMC are smaller, they are biased as the ones of the other two methods.

4.4 | Test 4: Calibrations on Clinical Data

In this section, we apply the calibration procedures to clinical data from two real patients affected by COVID-19-related pneumonia (Table 6). Centro Cardiologico Monzino in Milan and L. Sacco Hospital provided the data.

Since the parameter ranges for COVID-19-related pneumonia differ from those in the previous sections (see Appendix A), the GSA results also change. For brevity, we do not report the Sobol indices here, but only the parameters selected for calibration. Based on the GSA (as described at the beginning of Section 4), we choose the following parameters for the calibration for the patient from Monzino EA_{LV}, EA_{RV}, R^{SYS}_{AR}, C^{SYS}_{AR} and R^{SYS}_{VEN}. For the patient from Sacco Hospital, who has more clinical data available, the selected parameters are: EB_{LA}, EA_{LV}, EB_{LV}, EA_{RV}, R^{SYS}_{AR}, C^{SYS}_{AR} and R^{SYS}_{VEN}. We compare the estimated parameters and the ventricular PV (Pressure-Volume) loops which provide clinical insight into the patients' cardiac condition.

All *rRMSE* are less than 10^{-1} (Table 7), indicating successful calibration procedures. For both patients, CMC-L-BFGS-B and L-BFGS-B obtained the best results in terms of the loss function.

For the patient from Monzino, the relative standard deviations of the estimated parameters across the three calibration methods are less than 10% (Table 8), suggesting comparable estimates. L-BFGS-B and CMC-L-BFGS-B estimate the same parameter values except for EA_{RV}. Consequently, the left ventricular PV loops are nearly identical for these two calibration methods, while the right ventricular PV loops show greater differences (Figure 14a,b). CMC returns different estimates for the vascular parameters compared to the other two calibration methods, leading to clinically negligible differences in the PV loops. Despite only knowing the value of max ∇P_{rAV}, related to the right ventricle, all three calibration methods consistently indicate an

TABLE 6 | Clinical data of two patients, provided by Centro Cardiologico Monzino and L. Sacco Hospital in Milan.

Patient	HR	LA_{Vmax}	LV_{EDV}	LV_{ESV}	LV_{EF}	$\max \nabla P_{\text{rAV}}$	SAP_{max}	SAP_{min}	PAP_{max}
Monzino	70	—	233	130	42	25	140	55	—
Sacco	60	50	110	33	70	20	135	70	25

TABLE 7 | Final value of the *rRMSE* for the three patient-specific calibration methods.

Patient	CMC	L-BFGS-B	CMC-L-BFGS-B
Monzino	$5.4 \cdot 10^{-2}$	$4.0 \cdot 10^{-2}$	$3.8 \cdot 10^{-2}$
Sacco	$4.0 \cdot 10^{-2}$	$1.2 \cdot 10^{-2}$	$1.2 \cdot 10^{-2}$

TABLE 8 | Estimated parameters by the patient-specific calibrations and their relative standard deviations. For the Monzino patient, we do not calibrate EB_{LA} and EB_{LV} according to the GSA.

Patient	Calibration method	EB_{LA}	EA_{LV}	EB_{LV}	EA_{RV}	$R_{\text{AR}}^{\text{SYS}}$	$C_{\text{AR}}^{\text{SYS}}$	$R_{\text{VEN}}^{\text{SYS}}$
Monzino	CMC	—	1.04	—	0.66	0.62	0.65	0.27
	L-BFGS-B	—	1.02	—	0.66	0.55	0.75	0.24
	CMC-L-BFGS-B	—	1.02	—	0.60	0.55	0.75	0.23
Relative standard deviation		—	1%	—	5%	7%	8%	8%
Sacco	CMC	0.21	4.18	0.067	0.62	0.63	1.08	0.301
	L-BFGS-B	0.18	4.38	0.061	0.72	0.60	0.89	0.299
	CMC-L-BFGS-B	0.19	4.35	0.061	0.72	0.60	0.90	0.297
Relative standard deviation		7%	2%	6%	8%	3%	11%	1%

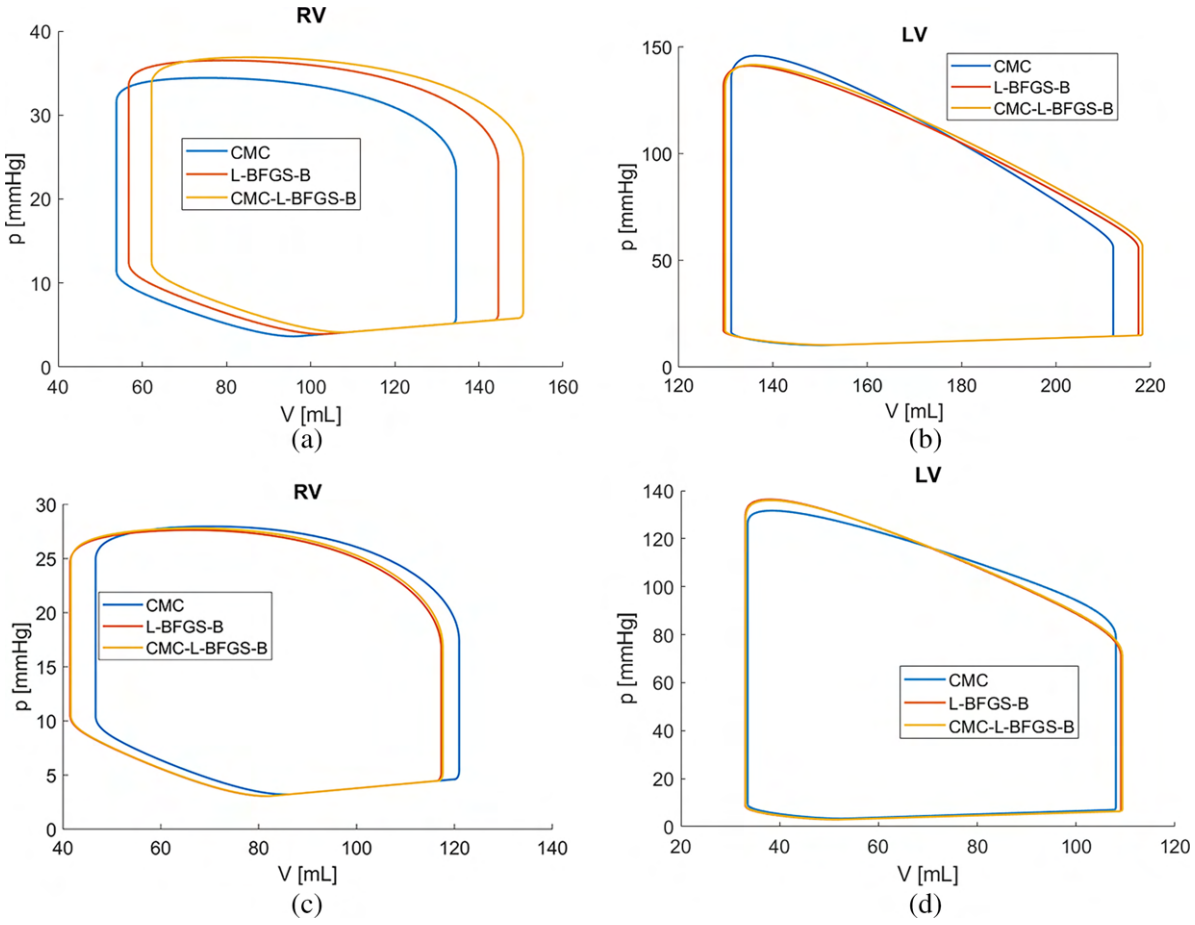

FIGURE 14 | Test 4. Estimated right ventricular (a) and left ventricular (b) PV loops of the Monzino patient and right ventricular (c) and left ventricular (d) PV loops of the Sacco patient.

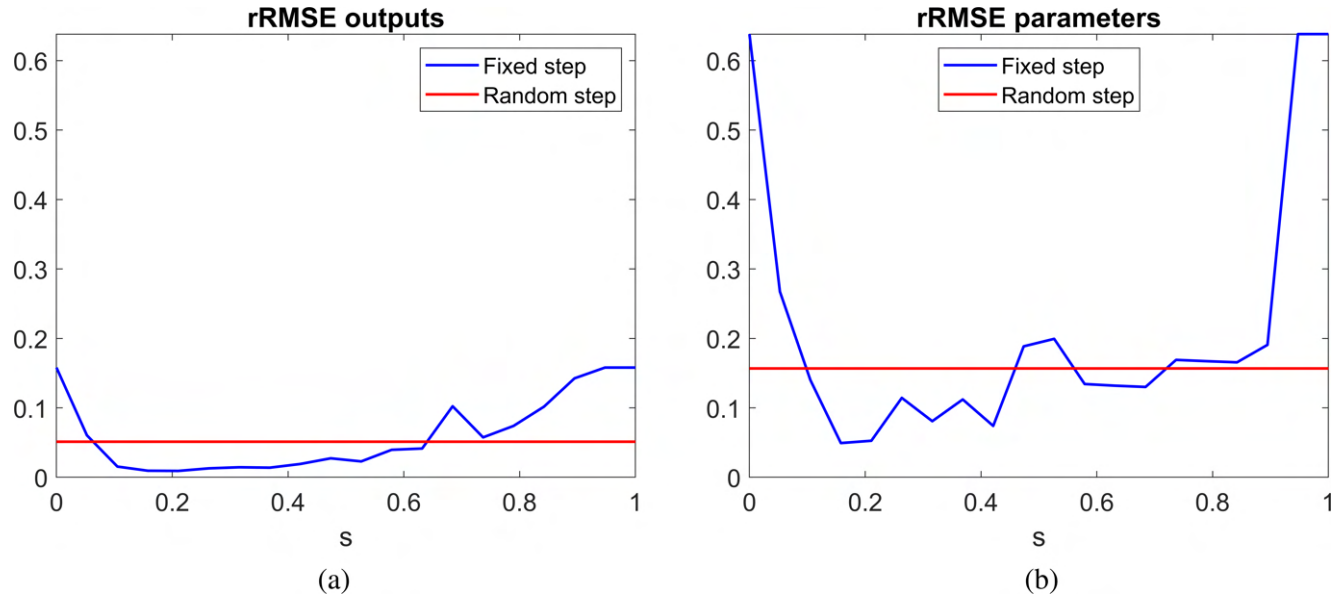

FIGURE 15 | Test 5. Relative root mean squared error between actual and estimated outputs (a) and parameters (b) varying the step size of the *calibrate* subroutine. The red lines represent the error achieved using a random step.

increased right workload, as evidenced by the RV_{Pmax} values (all above 30 mmHg) exceeding the associated healthy range [38] (Table 2). However, RV_{Pmin} values (all below 8 mmHg) are within the healthy range (Table 2). For the left ventricle, LV_{ESV} values (all above 52 mL), LV_{Pmax} (all above 140 mmHg) and LV_{Pmax} (all above 9 mmHg) are higher than the associated healthy ranges (Table 2), indicating an impaired left ventricular function. Due to the lack of BSA data, we can not compare RV_{EDV}, RV_{ESV} and LV_{EDV} values to the indexed healthy ranges (Table 2).

For the patient from L. Sacco Hospital, the relative standard deviations of the estimated parameters are less than 12% (Table 8) and the discrepancies in PV loops are smaller than in the previous case (Figure 14c,d), due to the availability of more clinical data. The three right and left ventricular PV loops indicate that despite being affected by COVID-19-related pneumonia, the patient is in healthy conditions.

4.5 | Test 5: Effects of Fixed Steps on the Correlation Matrix Calibration Method

In this section, we investigate the impact of different fixed step values s in the *calibrate* subroutine (described in Section 3.2), replacing the random step. We focus on calibrating patient one from Table 4 and run 20 tests with 20 evenly spaced steps in $[0, 1]$. At each iteration of CMC, we select a parameter $p_{\bar{1}}$ for calibration (as outlined in Section 3.2) and the *calibrate* subroutine updates $p_{\bar{1}}$ as $(1-s)p_{\bar{1}} + s\bar{b}$ if $p_{\bar{1}}$ needs to decrease or $(1-s)p_{\bar{1}} + s\bar{u}$ if it needs to increase, rather than sampling from a uniform distribution.

The *rRMSE* on outputs exhibits a decreasing trend as s increases from 0 to approximately 0.2 (Figure 15a). Above this threshold, the error increases. For $s = 0$ the optimal output estimate does not change since $(1-s)p_{\bar{1}} + s\bar{b} = (1-s)p_{\bar{1}} + s\bar{u} = p_{\bar{1}}$. When s approaches 1, the calibration procedure fails to improve the parameter estimates from the initial guess, resulting in an *rRMSE* on outputs equal to that for $s = 0$. The trend of the *rRMSE* on the parameters mirrors that for the outputs (Figure 15b). CMC is robust to the step size s, except for high and low values, with an optimal step size near 0.2. Using a random step in the *calibrate* subroutine leads to a suboptimal *rRMSE*. However, the tuning of the step size value requires different calibration simulations to perform the grid search.

5 | Conclusions

This study introduces two novel gradient-free calibration methods for a cardiocirculatory mathematical model based on the correlation matrix between model parameters and outputs. All the considerations are specific to the cardiocirculatory model presented in Section 2.

We showed that the new method, named CMC, outperforms L-BFGS-B in terms of successful calibrations (Section 4.1). Due to its random step procedure, CMC avoids local minima and explores the parameter space more efficiently than L-BFGS-B. This advantage also benefits the performance of the combined CMC-L-BFGS-B, which similarly outperforms L-BFGS-B in the number of successful calibrations. However, as a gradient-free method, CMC's estimates of cardiocirculatory parameters are less accurate than those of L-BFGS-B (Figures 5b and 7). Despite these differences, the PV loops obtained for real patients indicate the same cardiac condition (Section 4.4). We also showed that optimizing the calibration step values for CMC, at the expense of increased computational cost, can improve parameter estimates (Section 4.5).

In terms of computational time, CMC outperforms both L-BFGS-B and CMC-L-BFGS-B, offering a good trade-off between accuracy and efficiency in estimating clinical data for the cardiocirculatory model (Table 5). For sample 9 (Table 4), CMC is the most robust method among the three to the initial guess

of cardiocirculatory parameters (Section 4.2). However, this property is not consistent across all samples: for instance, repeating test 2 on sample 7, both L-BFGS-B and CMC-L-BFGS-B achieve relative root mean squared errors on the parameters of order 10^{-3}, while CMC's errors are more significant. Nonetheless, both CMC and CMC-LBFGS-B achieve results comparable to L-BFGS-B, even when dealing with noisy cardiovascular data (Section 4.3), making them viable alternatives.

We now address the limitations of this work.

Firstly, the assumption of parameter independence allows to use of Sobol's indices for the GSA. Removing this assumption and employing a sensitivity analysis method not require parameter independence would enhance the robustness of the analysis.

Secondly, the stopping criterion of CMC $\mathbf{a} = \mathbf{0}$ is never met. A more refined stopping criterion could potentially reduce the number of loss function evaluations and shorten the computational time to converge, as discussed in Section 4.1.

Thirdly, the use of correlation coefficients in CMC may overlook strong non-linear relationships between model parameters and outputs. To address this, we implemented CMC-L-BFGS-B, which incorporates L-BFGS-B steps to account for non-linear relationships. However, CMC-L-BFGS-B exhibits a lower convergence rate compared to the other two calibration methods. Fine-tuning the *rMSE* threshold (currently set to $2.5 \cdot 10^{-2}$), which triggers the switch from CMC to L-BFGS-B, could potentially improve the performances of CMC-L-BFGS-B.

Finally, in Sections 4.2, 4.3 and 4.5, we focused our analysis on a single sample. We verified that the results were independent from the specific sample by conducting the three tests of these sections on a few different samples. However, a more comprehensive analysis is needed to generalize our conclusions.

Acknowledgments

Andrea Tonini, Francesco Regazzoni, Luca Dede', Christian Vergara, and Alfio Quarteroni are members of the INdAM group GNCS "Gruppo Nazionale per il Calcolo Scientifico" (National Group for Scientific Computing). Andrea Tonini, Francesco Regazzoni, and Luca Dede' acknowledge the INdAM GNCS project CUP E53C23001670001. Francesco Regazzoni has been supported by the INdAM GNCS Project E53C22001930001 and by the project PRIN2022, MUR, Italy, 2023–2025, P2022N5ZNP "SIDDMs: shape-informed data-driven models for parametrized PDEs, with application to computational cardiology'". Christian Vergara and Luca Dede' would like to acknowledge the Italian Ministry of University and Research (MIUR) within the PRIN (Research projects of relevant national interest) MIUR PRIN22-PNRR n. P20223KSS2 "Machine learning for fluid-structure interaction in cardiovascular problems: efficient solutions, model reduction, inverse problems". Christian Vergara would like to acknowledge the Italian Ministry of Health within the PNC PROGETTO HUB-DIAGNOSTICA AVANZATA (HLS-DA) "INNOVA", PNC-E3-2022-23683266. The present research is part of the activities of "Dipartimento di Eccellenza 2023–2027", MUR, Italy, Dipartimento di Matematica, Politecnico di Milano.

Consent

Each patient provided consent to use his/her data for observational studies.

Conflicts of Interest

The authors declare no conflicts of interest.

Data Availability Statement

The data that support the findings of this study are available from the corresponding author upon reasonable request.

References

1. Y. Shi, P. Lawford, and R. Hose, "Review of Zero-d and 1-d Models of Blood Flow in the Cardiovascular System," *Biomedical Engineering Online* 10 (2011): 1–38.

2. A. Quarteroni, A. Veneziani, and C. Vergara, "Geometric Multiscale Modeling of the Cardiovascular System, Between Theory and Practice," *Computer Methods in Applied Mechanics and Engineering* 302 (2016): 193–252.

3. L. Dedè, F. Regazzoni, C. Vergara, et al., "Modeling the Cardiac Response to Hemodynamic Changes Associated With COVID-19: A Computational Study," *Mathematical Biosciences and Engineering* 18, no. 4 (2021): 3364–3383.

4. L. G. Fernandes, P. R. Trenhago, R. A. Feijóo, and P. J. Blanco, "Integrated Cardiorespiratory System Model With Short Timescale Control Mechanisms," *International Journal for Numerical Methods in Biomedical Engineering* 37, no. 11 (2021): e3332.

5. C. De Lazzari, M. Darowski, G. Ferrari, D. M. Pisanelli, and G. Tosti, "Modelling in the Study of Interaction of Hemopump Device and Artificial Ventilation," *Computers in Biology and Medicine* 36, no. 11 (2006): 1235–1251.

6. Y. Shi and T. Korakianitis, "Numerical Simulation of Cardiovascular Dynamics With Left Heart Failure and In-Series Pulsatile Ventricular Assist Device," *Artificial Organs* 30, no. 12 (2006): 929–948.

7. A. Tonini, C. Vergara, F. Regazzoni, et al., "A Mathematical Model to Assess the Effects of COVID-19 on the Cardiocirculatory System," *Scientific Reports* 14, no. 1 (2024): 8304.

8. G. Zhu, S. Modepalli, M. Anand, and H. Li, "Computational Modeling of Hypercoagulability in COVID-19," *Computer Methods in Biomechanics and Biomedical Engineering* 26, no. 3 (2023): 338–349.

9. J. Herrmann, V. Mori, J. H. T. Bates, and B. Suki, "Modeling Lung Perfusion Abnormalities to Explain Early COVID-19 Hypoxemia," *Nature Communications* 11, no. 1 (2020): 4883.

10. R. Laubscher, J. Van Der Merwe, P. Herbst, and J. Liebenberg, "Estimation of Simulated Left Ventricle Elastance Using Lumped Parameter Modelling and Gradient-Based Optimization With Forward-Mode Automatic Differentiation Based on Synthetically Generated Noninvasive Data," *Journal of Biomechanical Engineering* 145, no. 2 (2023): 021008.

11. R. H. Byrd, P. Lu, J. Nocedal, and C. Zhu, "A Limited Memory Algorithm for Bound Constrained Optimization," *SIAM Journal on Scientific Computing* 16, no. 5 (1995): 1190–1208.

12. C. Zhu, R. H. Byrd, P. Lu, and J. Nocedal, "Algorithm 778: L-BFGS-B: Fortran Subroutines for Large-Scale Bound-Constrained Optimization," *ACM Transactions on Mathematical Software (TOMS)* 23, no. 4 (1997): 550–560.

13. N. L. Bjørdalsbakke, J. T. Sturdy, D. R. Hose, and L. R. Hellevik, "Parameter Estimation for Closed-Loop Lumped Parameter Models of the Systemic Circulation Using Synthetic Data," *Mathematical Biosciences* 343 (2022): 108731.

14. N. L. Bjørdalsbakke, J. Sturdy, E. M. L. Ingeström, and L. R. Hellevik, "Monitoring Variability in Parameter Estimates for Lumped Parameter Models of the Systemic Circulation Using Longitudinal Hemodynamic Measurements," *Biomedical Engineering Online* 22, no. 1 (2023): 34.

15. N. L. Bjørdalsbakke, J. Sturdy, U. Wisløff, and L. R. Hellevik, "Examining Temporal Changes in Model-Optimized Parameters Using Longitudinal Hemodynamic Measurements," *Biomedical Engineering Online* 23, no. 1 (2024): 64.

16. H. V. Nguyen and T. Bui-Thanh, "Tnet: A Model-Constrained Tikhonov Network Approach for Inverse Problems," *SIAM Journal on Scientific Computing* 46, no. 1 (2024): C77–C100.

17. H. Saxton, T. Schenkel, I. Halliday, and X. Xu, "Personalised Parameter Estimation of the Cardiovascular System: Leveraging Data Assimilation and Sensitivity Analysis," *Journal of Computational Science* 74 (2023): 102158.

18. B. Efron and T. Hastie, *Computer Age Statistical Inference, Student Edition: Algorithms, Evidence, and Data Science*, vol. 6 (Cambridge, UK: Cambridge University Press, 2021).

19. W. R. Gilks and G. O. Roberts, "Strategies for Improving Mcmc," *Markov Chain Monte Carlo in Practice* 6 (1996): 89–114.

20. F. Argus, D. Zhao, T. P. Babarenda Gamage, M. P. Nash, and G. D. Maso Talou, "Automated Model Calibration With Parallel Mcmc: Applications for a Cardiovascular System Model," *Frontiers in Physiology* 13 (2022): 1018134.

21. D. M. Blei, A. Kucukelbir, and J. D. McAuliffe, "Variational Inference: A Review for Statisticians," *Journal of the American Statistical Association* 112, no. 518 (2017): 859–877.

22. H. Goh, S. Sheriffdeen, J. Wittmer, and T. Bui-Thanh, "Solving Bayesian Inverse Problems via Variational Autoencoders," arXiv preprint arXiv:1912.04212 (2019).

23. A. Saltelli, "Making Best Use of Model Evaluations to Compute Sensitivity Indices," *Computer Physics Communications* 145, no. 2 (2002): 280–297.

24. I. M. SobolÍ, "Sensitivity Estimates for Nonlinear Mathematical Models," *Mathematical Modeling and Computational Experiment* 1 (1993): 407.

25. M. Dandel, "Heart–Lung Interactions in COVID-19: Prognostic Impact and Usefulness of Bedside Echocardiography for Monitoring of the Right Ventricle Involvement," *Heart Failure Reviews* 27, no. 4 (2022): 1325–1339.

26. J. F. Park, S. Banerjee, and S. Umar, "In the Eye of the Storm: The Right Ventricle in COVID-19," *Pulmonary Circulation* 10, no. 3 (2020): 2045894020936660.

27. C. Diaz-Arocutipa, J. Saucedo-Chinchay, and E. Argulian, "Association Between Right Ventricular Dysfunction and Mortality in COVID-19 Patients: A Systematic Review and Meta-Analysis," *Clinical Cardiology* 44, no. 10 (2021): 1360–1370.

28. T. Mauri, E. Spinelli, E. Scotti, et al., "Potential for Lung Recruitment and Ventilation-Perfusion Mismatch in Patients With the Acute Respiratory Distress Syndrome From Coronavirus Disease 2019," *Critical Care Medicine* 48, no. 8 (2020): 1129–1134.

29. Q. Peng, X. Wang, and L. Zhang, "Chinese Critical Care Ultrasound Study Group (CCUSG)," Using Echocardiography to Guide the Treatment of Novel Coronavirus Pneumonia (2020).

30. F. Regazzoni, M. Salvador, P. C. Africa, M. Fedele, L. Dedè, and A. Quarteroni, "A Cardiac Electromechanical Model Coupled With a Lumped-Parameter Model for Closed-Loop Blood Circulation," *Journal of Computational Physics* 457 (2022): 111083.

31. S. Velthuis, V. M. Vorselaars, C. J. Westermann, R. J. Snijder, J. J. Mager, and M. C. Post, "Pulmonary Shunt Fraction Measurement Compared to Contrast Echocardiography in Hereditary Haemorrhagic Telangiectasia Patients: Time to Abandon the 100% Oxygen Method?," *Respiration* 89, no. 2 (2015): 112–118.

32. B. K. Saha, S. Ghalib, H. Chieng, et al., "Correlation of Respiratory Physiologic Parameters in Mechanically Ventilated Coronavirus Disease 2019 Patients," *Critical Care Explorations* 3, no. 1 (2021): e0328.

33. L. Gattinoni, S. Coppola, M. Cressoni, M. Busana, S. Rossi, and D. Chiumello, "COVID-19 Does Not Lead to a "Typical" Acute Respiratory Distress Syndrome," *American Journal of Respiratory and Critical Care Medicine* 201, no. 10 (2020): 1299–1300.

34. G. Q. Zhang and W. Zhang, "Heart Rate, Lifespan, and Mortality Risk," *Ageing Research Reviews* 8, no. 1 (2009): 52–60.

35. A. Albanese, L. Cheng, M. Ursino, and N. W. Chbat, "An Integrated Mathematical Model of the Human Cardiopulmonary System: Model Development," *American Journal of Physiology. Heart and Circulatory Physiology* 310, no. 7 (2016): H899–H921.

36. F. Liang, S. Takagi, R. Himeno, and H. Liu, "Multi-Scale Modeling of the Human Cardiovascular System With Applications to Aortic Valvular and Arterial Stenoses," *Medical & Biological Engineering & Computing* 47 (2009): 743–755.

37. R. M. Lang, L. P. Badano, V. Mor-Avi, et al., "Recommendations for Cardiac Chamber Quantification by Echocardiography in Adults: An Update From the American Society of Echocardiography and the European Association of Cardiovascular Imaging," *European Heart Journal Cardiovascular Imaging* 16, no. 3 (2015): 233–271.

38. J. W. Hurst, R. C. Schlant, C. E. Rackley, E. H. Sonnenblick, and N. K. Wenger, "The heart, arteries e veins," 1990.

39. L. G. Rudski, "Guidelines for the Echocardiographic Assessment of the Right Heart in Adults: A Report From the American Society of Echocardiography: Endorsed by the European Association of Echocardiography, a Registered Branch of the European Society of Cardiology, and the Canadian Society of Echocardiography," *Journal of the American Society of Echocardiography* 23, no. 7 (2010): 685–713.

40. I. M. Sobol, "On the Distribution of Points in a Cube and the Approximate Evaluation of Integrals," *Zhurnal Vychislitel'noi Matematiki i Matematicheskoi Fiziki* 7, no. 4 (1967): 784–802.

41. A. Saltelli, P. Annoni, I. Azzini, F. Campolongo, M. Ratto, and S. Tarantola, "Variance Based Sensitivity Analysis of Model Output. Design and Estimator for the Total Sensitivity Index," *Computer Physics Communications* 181, no. 2 (2010): 259–270.

42. M. D. Morris, "Factorial Sampling Plans for Preliminary Computational Experiments," *Technometrics* 33, no. 2 (1991): 161–174.

43. K. Pearson, "Vii. Note on Regression and Inheritance in the Case of Two Parents," *Proceedings of the Royal Society of London* 58, no. 347–352 (1895): 240–242.

44. J. Bradbury, R. Frostig, and P. Hawkins, "Jax: Composable Transformations of Python+NumPy Programs," 2018.

45. M. Salvador, F. Regazzoni, L. Dedè, and A. Quarteroni, "Fast and Robust Parameter Estimation With Uncertainty Quantification for the Cardiac Function," *Computer Methods and Programs in Biomedicine* 231 (2023): 107402.

Appendix A

Bounds on the Parameters

In this section, we outline the bounds of the parameter hypercube used in the GSA and the calibration procedures for the lumped-parameter cardiocirculatory model.

For the GSA, as described in Section 3.1, we fix the HR and cardiac cycle timings, modifying only the parameters in Table 1 as "parameters used in the global sensitivity analysis". We have previously chosen a reference setting of parameters $\mathbf{p}^{\mathrm{R}}$ (Table 1) to model an ideal healthy individual (Section 2). To account for variations among different healthy individuals, we allow the parameters to vary within a hypercube centered around $\mathbf{p}^{\mathrm{R}}$. The width in each direction is set to 2/3 of the reference

parameter value. We sample each parameter p_l $(1 \leq l \leq N_p = 32)$ in $\left[\left(1 - \frac{2}{3}\right)p_l^R, \left(1 + \frac{2}{3}\right)p_l^R\right]$. This hypercube width enables us to account for several possible conditions.

For the calibration methods, we fix at their reference value the parameters with total Sobol' indices all less than 0.1, as these parameters do not significantly affect the model outputs used for calibration (Table 2), making them non-identifiable. The remaining parameters are free to vary within the same ranges as those used in the GSA.

To account for severe COVID-19-related pneumonia, we consider three additional changes in the parameter ranges, according to clinical literature:

- The active elastances of the four cardiac chambers may be further halved to simulate reduced cardiac contractility, reflecting the impairment of the cardiac function due to the infection [25].
- The pulmonary resistances can be further triple to model varying levels of increased pulmonary resistances due to vascular wall thickening [28, 29].
- The pulmonary compliances can be further divided by 3 to account for potential endothelial damage, leading to decreased compliance [28].